University of Oslo, Department of Physics
Master's Thesis

Development and Calibration of a DSLR System for Auroral Studies.

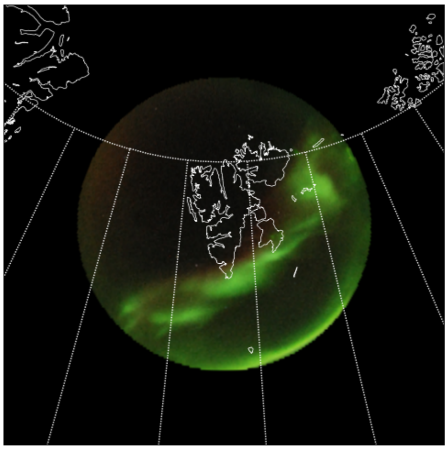

Nial Peters

March 2009

Abstract

In this thesis, a commercially available Nikon D80 digital single lens reflex camera (DSLR) equipped with a Sigma EX 4.5 mm circular fish-eye lens has been intensity calibrated to absolute units, in order to be used for auroral-related studies of the polar ionosphere. The spectral responsivity of the D80 was found using calibration equipment at the UNIS calibration lab, and shows that 6300 and 5577 auroral emissions are recorded by separate colour channels in the captured images. By assuming that these emissions dominate the recorded counts in these colour channels, calibrated images at these wavelengths have been produced. The spectral responsivity of the D80 was found to be $(1.4 \pm 0.04) \times 10^{-3} counts\ s^{-1}\ R^{-1}$ for 557.7 nm and $(6.9 \pm 0.05) \times 10^{-4} counts\ s^{-1}\ R^{-1}$ for 630.0 nm. Auroral optical emissions were recorded by the D80 at the Kjell Henriksen Observatory, and it was found that there was a good intensity agreement between data from the MSP and the calibrated D80 for auroral emissions. It was also found that the D80 is not sensitive enough at low intensities to detect polar cap patches. Any discrepancies in the data sets are attributed both to the difference in time resolution of the two instruments and elevated background light levels caused by high Sun elevation. In addition to the intensity calibration, work was put into the development of software for controlling the camera and also for processing the captured images. The image processing software has been designed to work with images from any all-sky imager to allow data comparisons to be easily performed.

Acknowledgements

The work presented in this thesis would not have been possible without the help and support of a large number of people. I would especially like to thank the following (in no particular order) for their contributions:

- My supervisors Dag Lorentzen and Jøran Moen for making this whole project possible.
- Jeff Holmes for “showing me the ropes” and for the large amount of time spent helping me out.
- The Leverhulme Trust, without whose financial support this project could not have gone ahead.
- Julian Todd for his expert programming advice.
- Fred Sigernes for his help with the calibration work, particularly in these last few weeks.

Furthermore, I would like to thank all the staff and students at UNIS. It truly is a unique place to study, and I will never forget the friends I have made and the experiences I have shared here.

Contents

List of Figures

1 Introduction

This thesis is an investigation into the possibility of using commercially available DSLR cameras as all-sky imager systems. Whilst focus is given to the Nikon D80 model of DSLR camera, the methods described can be easily generalised to many different models and brands.

Ground-based observations of the polar ionosphere provide data over a much larger spatial region than is possible using direct measurement techniques such as satellites or rockets. Such data is important in order to understand the many physical processes occurring in the ionosphere. These processes are not only interesting from a scientific perspective, providing a chance to study phenomena that are difficult to produce in a laboratory, but also have commercial interest. For example, a major factor influencing the accuracy of Global Positioning Systems (GPS), is the scintillation of the signal caused by the ionosphere.

Svalbard plays host to a large number of ground-based optical and radar instruments for ionospheric observation. Within the optical class, there are two instruments that are of particular importance: the meridian scanning photometer (MSP) and the all-sky imager (ASI). Data from ASIs is of particular interest since it provides a two dimensional view of auroral events.

Typically, all-sky imagers use a combination of a CCD sensor and an array of interference filters to image the sky at different wavelengths. The array of filters is usually mounted on a rotating filter wheel, allowing different filters to be easily aligned with the optical axis of the system. However, interference filters require that light be collimated before it passes through the filter. The collimated light must then be focused onto the sensor. Further complexity is added in intensified systems which require additional optics to focus the intensified image onto the sensor. The resulting instrument is not only large and costly, but also provides poor time resolution when used to image at multiple wavelengths. This is due to the time delay introduced by having to rotate the filter wheel.

The large consumer market for digital cameras has resulted in a rapid increase in quality coupled with a steady decrease in price. At the top end of most manufacturers' product ranges, Digital Single Lens Reflex (DSLR) cameras are capable of long exposure, high sensitivity imaging. As the name suggests, they use only a single lens element, which focuses incoming light onto a CCD (or CMOS) sensor via a Colour Filter Mosaic (CFM). The CFM ensures that each pixel on the CCD only records incoming light within a certain wavelength range. The colour value of any given pixel is then recreated post-capture by interpolating the values of the surrounding pixels. All pixels on the CCD record simultaneously, allowing a colour composite image to be captured within one exposure time. This, coupled with the low cost of DSLR cameras makes them an attractive alternative to custom built scientific imagers [Partamies et al., 2007].

Section 2 of this thesis gives a brief introduction to auroral physics. This is followed by a summary of the instrumentation used in Section 3. An overview of the image processing and DSLR control software developed is given in Section 4. Calibration techniques for converting image data into absolute intensity units (Rayleighs) are discussed in Section 5. Data captured during the 2007-2008 and 2008-2009 field seasons by a D80 situated at the Kjell Henriksen Observatory (KHO) on Svalbard is presented in Section 6, demonstrating its capabilities as an ASI system.

2 Theoretical Background

In order to appreciate the motivation behind this investigation, and understand the data presented in later sections, it is required that the reader have at least a basic grasp of auroral physics. This section outlines the important concepts, leaving out much of the in-depth detail in favour of clarity.

2.1 The Fluid Description of a Plasma

The fluid description of a plasma, more commonly referred to as magnetohydrodynamics or MHD, is perhaps the most frequently used plasma model in space physics. As the name suggests, it treats the plasma as a fluid, allowing average properties such as density and temperature to be determined over larger spatial volumes than is possible by considering single particle motion. The equations of MHD describe both the electromagnetic, and the mechanical properties of plasmas. As such, they are formed by combining Maxwell's equations of electrodynamics with the well known fluid dynamics equations of continuity and the Navier-Stokes equation. Ohm's law is also included.

The detailed derivation of the MHD equations is of little interest within the scope of this thesis. However, their assumptions and implications are crucial to the understanding of many of the mechanisms and phenomena presented in the following sections. It is therefore instructive to study the equations in some detail. The idealised equations of MHD are:

Maxwell's equations in the MHD limit:

From Faraday's law combined with Ohm's law:

$$\frac{\partial \mathbf{B}}{\partial t} = \nabla \times (\mathbf{v} \times \mathbf{B}) \tag{1}$$

where **B** is magnetic field strength and **v** is velocity.

From Ampère's law:

$$\nabla \times \mathbf{B} = \mu_0 \mathbf{j} \tag{2}$$

where μ_0 is the permeability of free space and **j** is current.

Fluid dynamics equations:

From the Navier-Stokes equation (momentum conservation):

$$\rho \frac{\partial \mathbf{u}}{\partial t} = -\nabla p + \mathbf{j} \times \mathbf{B} + \rho \mathbf{g} \tag{3}$$

where ρ is density, **u** is velocity, p is pressure and **g** is the acceleration due to gravity.

Continuity equation (mass conservation):

$$\frac{\partial \rho}{\partial t} + \nabla \cdot \rho \mathbf{u} = 0 \tag{4}$$

The regime in which these equations are valid, the MHD limit, requires that the temporal and spatial scales under consideration be large compared to those of microscopic motion in the plasma. For example $t \gg 1/\omega_c$ and $x \gg \lambda_D, r_L$ where ω_c is the cyclotron frequency, λ_D is the Debye length and r_L is the Larmor radius. Also required is charge neutrality, zero velocity, no collisions, small currents and no production or annihilation of plasma. Under these conditions, the ideal gas law may be applied to the plasma.

2.1.1 The Frozen-in Field Condition

Consider a volume of plasma moving with velocity **v** through a magnetic field **B**. The temporal variation of magnetic flux threading the volume (ϕ) can be written:

$$\frac{\partial \phi}{\partial t} = \int_S \frac{\partial \mathbf{B}}{\partial t} \cdot \mathbf{dS} + \oint \mathbf{B} \cdot \mathbf{v} \times \mathbf{dl} \tag{5}$$

where **S** is the bounding surface of the plasma volume and **l** is the surface boundary.

Using a combination of the Kelvin-Stokes theorem and the properties of the vector triple product, the second term of Eq. 5 can be rewritten in terms of a surface integral.

$$\frac{\partial \phi}{\partial t} = \int_S \frac{\partial \mathbf{B}}{\partial t} \cdot \mathbf{dS} - \nabla \times (\mathbf{v} \times \mathbf{B})\, \mathbf{dS} \tag{6}$$

In the MHD limit, the two terms on the right hand side cancel (see Eq. 1) and we are left with:

$$\frac{\partial \phi}{\partial t} = 0 \tag{7}$$

The magnetic flux threading the volume of plasma is constant in time. This is known as the frozen-in condition, since the magnetic flux lines can be thought of as being bound to the plasma. This has some important consequences when considering plasma motion in the solar wind. Plasma motion is bound to a single flux tube (defined as the spatial volume mapped out by following flux lines which cut a surface along their entire length). Essentially this means that plasma cannot move across closed field lines, only along them (Fig. 1). The frozen-in condition is valid when the magnetic Reynolds number is large compared to unity: $R_m \simeq \mu_0 \sigma u L \gg 1$ where u is the flow speed, σ is the conductivity and L is a characteristic length scale.

2.2 The IMF and Magnetic Reconnection

The huge pressure difference between interplanetary space and the solar corona drives a supersonic flow of solar plasma radially outwards from the Sun. Referred to as the solar wind, it consists primarily of electrons and protons in approximately equal numbers, with a small number of heavier ions. It is therefore almost electrically neutral. In accordance with the frozen-in field condition (Section 2.1.1), the solar wind carries with it a weak ($\sim 5nT$) magnetic field originating at the Sun. This field, termed the inter-planetary magnetic field or IMF, is relatively dynamic (as viewed from the Earth), and changes in both direction and strength.

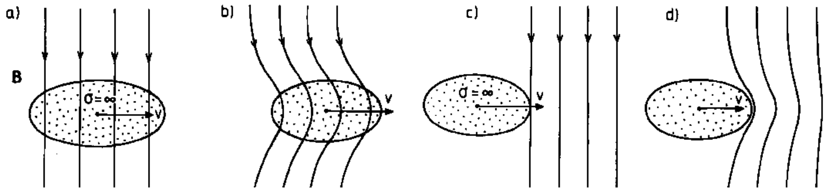

Figure 1: Visual interpretation of the frozen-in condition. (a) and (b) show how plasma motion can distort the flux tube that it is on. (c) and (d) show the distortion of a neighbouring flux tube, which the plasma cannot cross. Figure taken from Brekke [1997].

The direction of the IMF is most easily represented in GSM (Geocentric Solar Magnetospheric) coordinates. The GSM system has its origin situated at the centre of the Earth, with a positive x-direction towards the Sun. The z-axis lies parallel to the dipole axis of the Earth's magnetic field, with a positive z-direction towards the north. The y-axis lies perpendicular to both x and z axes with a positive y-direction towards dusk. The IMF is commonly classified by its components in this coordinate system, with southward (northward) IMF being used interchangeably with IMF $B_z < 0$ $(B_z > 0)$. The IMF direction may also be specified by its clock angle [Sandholt et al., 1998], defined as the angle from the z-axis of the projection of the IMF vector in the y-z plane with zero degrees clock angle corresponding to northward IMF.

The interaction between the Earth's magnetic field and the IMF is complex and varies with the relative orientation of the two fields. However, broadly speaking, the solar wind causes a compression of the Earth's magnetic field on the dayside and an elongation away from the Earth (the magnetotail) on the nightside. The (approximately) dipole field of the Earth is thus confined to a finite region of space known as the magnetosphere. Furthermore, the collision of the supersonic solar wind with a static object leads to the formation of a shock front on the dayside, the bow shock. Earthwards of the bow shock, the solar wind flows subsonically around the magnetosphere in a region called the magnetosheath. The transition region between dominance of the IMF and dominance of the Earth's magnetic field is known as the magnetopause.

2.2.1 Magnetic Reconnection

The frozen-in field condition discussed in Section 2.1.1 states that plasma with a high magnetic Reynolds number is bound to a single magnetic flux tube. A consequence of this is that plasma on different flux tubes cannot mix, permitting large discontinuities in plasma properties across flux tubes.

The magnetic fields making up the neighbouring flux tubes may differ in both direction and field strength. In accordance with Ampère's law (Eq. 2), the boundaries between differing flux tubes contain current sheet systems. The boundary current sheets are thin in relation to the flux tubes that they separate. The relatively small length scale within the boundary layer reduces the magnetic Reynolds number to the extent that the frozen-in field condition is no longer valid. This breakdown is known as magnetic reconnection.

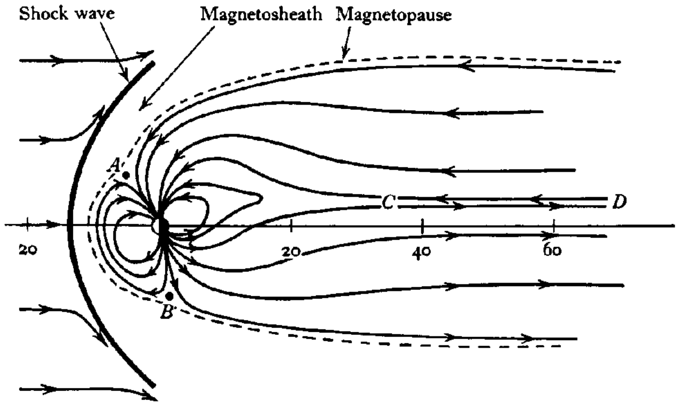

Figure 2: Midday-midnight cross-section of the Earth's magnetosphere; the Sun is to the left. Figure taken from Brekke [1997].

A simple model of magnetic reconnection is provided by the x-type neutral line model. In this model, reconnection occurs along a single line. Consider the boundary between two flux tubes with anti-parallel magnetic fields, Fig. 3. Ampère's law (Eq. 2) requires current flow (and therefore an electric field) perpendicular to both magnetic fields. By considering the Lorentz force, we can see that plasma in both flux tubes is accelerated towards the centre of the boundary region, towards the line of zero magnetic field (x-type neutral line). Within this central region, known as the diffusion region, the frozen-in condition breaks down. Magnetic field lines from the two flux tubes are cut, and rejoin with each other. Plasma is then accelerated outwards from the diffusion region parallel to the boundary layer.

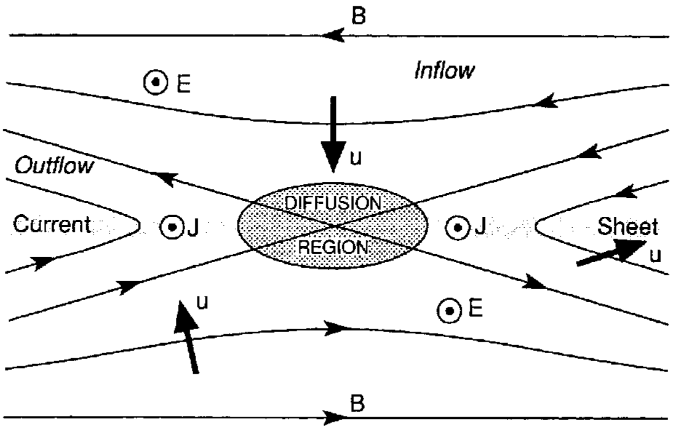

Figure 3: Schematic of the x-type neutral line reconnection mechanism at the boundary between anti-parallel magnetic fields. Figure taken from Kivelson and Russel [1995].

The most important consequence of magnetic reconnection is that it permits mixing of plasma across flux tubes. The boundary between flux tubes is no longer closed, instead plasma can traverse it, following field lines that have been reconnected across it. Such field lines are referred to as open field lines, whereas field lines that close on themselves (within a single flux tube) are known as closed field lines. In the context of the Sun-Earth system, open field lines are those that are tied at one end to the Earth, and at the other to the IMF (ultimately the Sun).

2.2.2 Convection

If we consider the IMF to be southward (such that it is anti-parallel to the Earth's magnetic field at the magnetopause), we can see that reconnection between the two fields is possible. The extended and anti-parallel field in the centre of the magnetotail is also a candidate site for reconnection. It was proposed by Dungey [1961] that observed plasma flows across the polar cap could be accounted for by reconnection at these two sites. Reconnection at the magnetopause forms a pair of open field lines, one in each hemisphere. Plasma motion in the solar wind drags (due to the frozen-in condition) these field lines from the dayside, across the polar cap and into the nightside; stretching them out into the magnetotail. In the magnetotail, the open field lines from both hemispheres can reconnect, forming closed field lines in both the IMF and the Earth's magnetic field. The entire process is more clearly represented in Fig. 4.

Often referred to as convection, the motion of plasma across the polar cap is highly dependent on the direction of the IMF. Reconnection is favoured by a southward IMF, with IMF B_y components affecting the shape of the convection cells. It should be noted however, that reconnection still occurs for IMF $B_z > 0$, but it is thought to take place further towards the magnetotail than for IMF $B_z < 0$.

2.3 The Aurora

2.3.1 Electronic Transitions

It is known from quantum mechanics (see for example Rae [2002]) that the electrons of an atom, ion or molecule may only occupy certain energy levels. These levels, and therefore the energies between them, are specific to the species under consideration. The energy transferred during the transition of an electron from one level to another is therefore a useful identifier of the parent species.

Electronic transitions are governed by a set of selection rules. These require properties of the electronic state, such as angular momentum and spin, to change by certain amounts between energy levels. Transitions between energy levels which do not fulfil the selection rules are known as forbidden transitions. Whilst these transitions still occur, they are considerably less likely than allowed transitions and as a result the electron has a much greater lifetime in its initial state. For example, an electron may occupy a high energy, excited state for a much greater period of time than would be expected, if the required transition to lower energy violates the selection rules.

An electronic transition to a higher energy level may be caused by a collision between a fast moving ion and the parent species. In this case, some of the ion's kinetic energy is transferred to the electron, promoting it to a higher energy

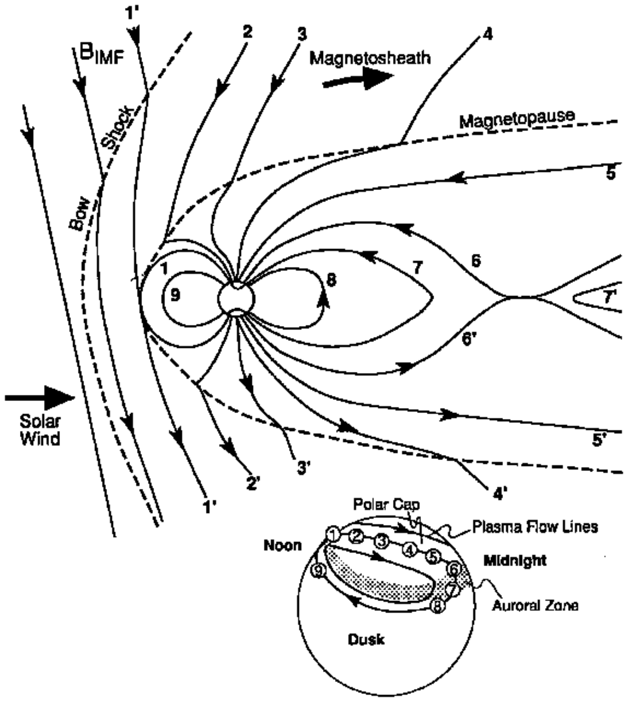

Figure 4: Schematic of the reconnection-driven polar convection cycle. Reconnection at the magnetopause creates a pair of open field lines (1). The solar wind drags the open field lines across the polar caps and into the magnetotail (2-5). Open field lines reconnect in the magnetotail to form closed field lines (6-7). Closed field lines return to the dayside around the edge of the polar cap (8-9). Figure taken from Kivelson and Russel [1995].

level, otherwise known as an excited state. The excited electron may return to a lower energy level by the emission of a photon. The energy (and therefore wavelength since $E_{photon} = h\nu$, where h is Planck's constant and ν is frequency) of the emitted photon is equal to the energy gap between the two electronic states of the transition. Alternatively, further collisions may return the electron to a lower energy through a process known as collisional quenching. The longer lifetime of excited states decaying via forbidden transitions means that they are more prone to collisional quenching.

2.3.2 Auroral Emissions

The reconnection processes described in Section 2.2.2, allow plasma to enter the Earth's atmosphere along flux tubes. Following dayside reconnection, the Earth's magnetic field is joined to the IMF, allowing plasma directly from the solar wind to flow down open field lines into the atmosphere. On the nightside, reconnection of open field lines from both hemispheres accelerates plasma from the centre of the magnetotail (the central plasma sheet) both towards and away from the Earth. That which is accelerated towards the Earth is able to enter the atmosphere on closed field lines. The consequences of these different mechanisms for dayside and nightside particle injection is discussed more in Section 2.3.3. This section deals with particle precipitation in more general terms.

The plasma entering the atmosphere is predominantly made up of protons and electrons. Whilst precipitating protons do produce auroral emissions, this thesis focuses on electron aurora and proton aurora will not be mentioned further. Electrons precipitating through the atmosphere invariably collide with atmospheric constituents, losing energy with each collision and ending up as thermal electrons. As outlined in Section 2.3.1, these collisions can cause electronic excitations, and the subsequent photo-relaxation of the electron is what produces auroral emissions.

The aurora is made up of a number of almost monochromatic[1] emissions at various wavelengths, each resulting from a particular transition within different atmospheric molecules. The visible aurora is dominated by three key emissions:

The 6300Å emission is due to an atomic Oxygen transition:

$$O(^3P) + e \rightarrow O(^1D) + e' \rightarrow O(^3P) + e' + h\nu$$

The 5577Å emission is also due to an atomic Oxygen transition:

$$O(^3P) + e \rightarrow O(^1S) + e' \rightarrow O(^1D) + e' + h\nu$$

The 4278Å emission is due to an ionised molecular Nitrogen transition:

$$N_2 + e \rightarrow (N_2^+)^* + e' + e_n \rightarrow N_2^+ + e_n + e' + h\nu$$

Two of these emissions are shown in Fig. 5. What is clear from the figure is that the emissions are, to a large extent, separated spatially. In fact, the separation is in altitude. The peak emission altitude depends on both the atmospheric density and the penetration depth of the precipitating electrons. The mean energy of the precipitating electrons increases with altitude, whereas atmospheric density falls off exponentially. Lower density means fewer collisions, and therefore less excitations at high altitudes. However, a higher average electron energy means that a greater number of collisions will have sufficient energy to cause excitations. These competing effects combine to give a relatively broad peak in emission intensities as shown in Fig. 6.

Higher energy transitions are expected to peak at higher altitudes, since they require higher energy precipitating electrons. However, as Fig. 6 shows, this is not what is observed. The atomic Oxygen transitions are forbidden transitions, and as such are relatively stable in their excited states. The long lifetimes (0.7 seconds and 110 seconds for 5577Å and 6300Å respectively) of the excited states makes them more vulnerable to collisional quenching. As the probability of quenching increases with atmospheric density, the peaks in emission are observed at considerably higher altitudes than the peaks in excitation probability.

---

[1] Whilst the energy gap between electronic states is perfectly quantised, thermal motion causes a Doppler broadening of the emission.

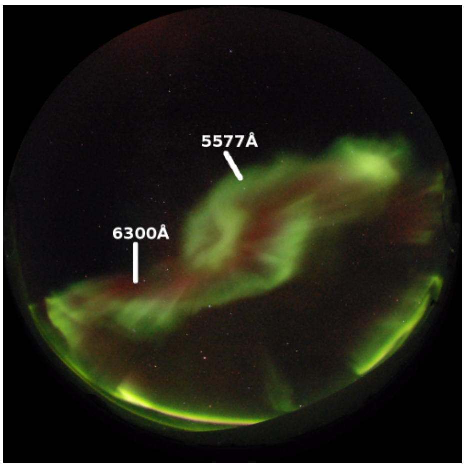

Figure 5: All-sky image from the Nikon D80 DSLR camera at the Kjell-Henriksen Observatory, recorded at 18:48 UT on 1st February 2008, showing the separation of the 5577Å and the 6300Å auroral emissions. Image recorded at 20s exposure time, F2.8 and ISO 1600.

2.3.3 Dayside/Nightside Aurora

As shown in Fig. 6, there are considerable differences between dayside and nightside emission profiles. This should come as no suprise given the very different mechanisms for each.

Dayside emissions are caused by precipitating particles on open field lines. The direct connection between the IMF and the Earth's magnetic field allows particles directly from the solar wind to enter the atmosphere. Typically these particles are of lower energy (¡1 keV) than those found on the nightside [Deehr et al., 1980], and consequently do not penetrate to such low altitudes. Hence, dayside aurora has lower intensity emissions at 5577Å and 4278Å . The relatively high flux of precipitating particles results in a higher intensity of 6300Å emissions than on the nightside.

In contrast, nightside emissions are caused by particles entering the atmosphere on closed field lines. Reconnection in the magnetotail accelerates particles from the central plasma sheet into the atmosphere. These particles have a relatively high energy (0.5-20 keV), penetrating to low altitudes and producing far higher intensity 5577Å and 4278Å emissions than found on the dayside.

2.3.4 Precipitation Regions

The region where particles enter the atmosphere along magnetic field lines (as described in Section 2.3.3) is known as the auroral oval. The shape of the auroral oval is highly dependent on solar activity. However, the oval on the dayside is typically compressed and much narrower than the nightside oval. The oval is centred around the geomagnetic pole, with an average position of $\sim 75°$MLAT (magnetic latitude) on the dayside and $\sim 67°$MLAT on the nightside. Within the auroral oval, there are many different precipitation regions relating to the mappings along field lines of different sources of plasma. The

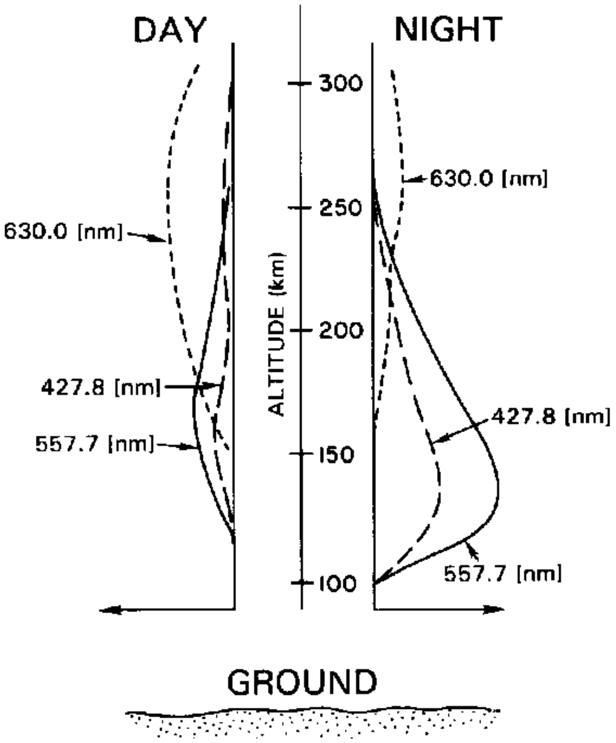

Figure 6: Emission intensity profiles with altitude for 4278Å, 5577Å and 6300Å, for both dayside and nightside aurora. Figure taken from Kivelson and Russel [1995].

energy and density of precipitating particles varies across these regions, producing different emission spectra. The detailed specifications of these regions is of little importance within the scope of this thesis, which only focuses on dayside/nightside comparisons. For a more complete explanation the reader is referred to the work of Newell et al. [2004].

The Kjell Henriksen Observatory is located at ∼ 75.1°MLAT. It is therefore within the dayside auroral oval, making it an ideal location to study dayside aurora. However, for nightside observations, it is too far north. Nightside aurora is only observed at KHO during periods of magnetospheric disturbance, known as substorms.

The exact sequence of events leading to a substorm is still an open topic for debate. However, the general concensus is that an unstable magnetotail (either due to plasma build up or temperature rise) is perturbed somehow, possibly by a change in the IMF. The perturbation triggers rapid reconnection, producing earthward jets of plasma from the central plasma sheet. The plasma jet causes both magnetospheric disturbances and an expansion of the auroral oval. It is this expansion which allows nightside aurora to be observed from KHO.

2.4 Polar Cap Patches

Polar cap patches are regions of enhanced electron density ranging in size between 100-1000km [Crowley, 1996]. They are typically found at an altitude of around 300km [Lorentzen et al., 2004]. Originating on the dayside, they are pulled (due to the frozen-in condition, Section 2.1.1) across the polar cap by convecting field lines, and into the nightside auroral oval.

The formation mechanism for polar cap patches is still not fully understood. However, it is believed that the source of plasma for most patches is a "tongue of ionisation" (TOI) stretching from low latitudes, through the dayside auroral oval and towards the polar cap [Knudsen, 1974]. The TOI is thought to be due to ionisation of the sunlit ionosphere by solar extreme ultra-violet radiation.

Polar cap patches can be observed using radar (for example [Oksavik et al., 2006]) due to their high density. Optically they can be observed as patches of weak airglow at 630.0 nm due to recombination of atomic Oxygen.

3 Additional Instrumentation

In order to assess the effectiveness of the Nikon D80 as an ASI system, data captured during its two field seasons of operation is compared with that from several other optical instruments (Section 6). This section gives a brief introduction to these instruments and their capabilities. The Fixed Imaging Compact Spectrograph (FICS), which was used extensively during the calibration of the D80, is also introduced.

3.1 Meridian Scanning Photometer

The Meridian Scanning Photometer (MSP) at KHO records intensities along the geomagnetic meridian plane on five channels simultaneously. In its current configuration it records at 630.0 nm, 427.8 nm, 557.7 nm, 486.1 nm and 656.0 nm. For each channel, there is a separate filter, filter tilter and photomultiplier tube. A mirror, mounted in front of the filters, rotates in the geomagnetic meridian plane beneath a perspex slit in the observatory. This gives a 180 degree field of view.

The filters used in the MSP are interference filters and the wavelength they transmit therefore depends on the incident angle of the radiation. This property is utilized by the MSP, tilting the filters in order to record both peak and background emissions.

The photomultiplier tubes (PMTs) convert the incoming light into an electrical pulse. Each photon entering the tube releases a single electron via the photoelectric effect. This electron is directed onto a dynode which releases multiple electrons. These in turn are directed onto further dynodes producing a large cascade of electrons, which are collected at the anode and form the output signal. Calibration using a calibration lamp and a diffuse re-emitting screen is needed to convert the output voltages of the PMTs into absolutely calibrated intensity data.

In normal operation, one complete MSP scan consists of four scans of the meridian. On two of these scans the filter tilters angle the filters to allow radiation of the desired wavelength through (the peak intensity). The base intensity is measured by changing the filter angles (and therefore wavelengths) away from the desired values and recording the background levels. This is also done for two scans and then the two sets of peak-base values are averaged to give the final result. The complete set of four scans can be done once every 16 seconds.

3.2 UiO All-sky Imager

The UiO ASI at KHO is an intensified, filter wheel type imager. Narrow band (2nm bandwidth) interference filters are mounted in a filter wheel, and rotated into alignment in order to record at different wavelengths. It is currently equipped with 4278Å , 5577Å and 6300Å filters. A circular fish-eye lens is used as entrance optics giving a 180 degree field of view. However, mountains and other instrument domes partly obscure the sky close to the horizon. Images are therefore usually cropped at 75 degrees from zenith.

3.3 Auroral Spectrograph

Operated by the Japanese National Institute of Polar Research, the Auroral Spectrograph (ASG) at KHO records intensity data between 420-740 nm with a resolution of 0.6 nm. It has a 180 degree field of view along the geomagnetic meridian, giving a good overview of auroral emissions over the entire sky. Coupled with its relatively wide wavelength range this makes it a very useful instrument for comparisons with ASI data.

3.4 Fixed Imaging Compact Spectrograph (FICS)

Manufactured by ORIEL, the SN7743 Fixed Imaging Compact Spectrograph (FICS) has a spectral range of 4000-11000Å and a bandpass of 96Å. The field of view of the FICS is 22°. For the calculation of the D80's spectral responsivity, the FICS was used in conjunction with a filter to remove second order components.

The FICS was calibrated using the method described by Sigernes et al. [2007]. A 45W Tungsten lamp is used to illuminate a diffuse re-emitting screen (with a reflectance of 0.99) at a distance of 8.554m. The FICS (with the filter attached) is mounted such that the screen fills its field of view. A background-subtracted scan with a four second exposure is recorded by the FICS. The recorded counts are compared to the known intensity of the lamp at different wavelengths. Eq. 8 is then used to calculate the factors needed to convert raw counts to R/Å.

$$K_\lambda = 4 \times 10^{-6} B_{0\lambda} \left(\frac{z_0}{z}\right)^2 \rho \cos(\alpha) \frac{1}{C_\lambda} \tag{8}$$

where K_λ is the calibration factor at wavelength λ in $[R\,\text{Å}^{-1} counts^{-1}]$. $B_{0\lambda}$ is the known radiance of the lamp (from the certificate) in $[photons\ cm^{-2}s^{-1}\text{Å}^{-1}]$ obtained at a distance of $z_0 = 0.5m$. z is the lamp-screen distance (8.554m), ρ is the screen reflectance (0.99), α is the lamp-screen angle (0°) and C_λ is the recorded counts at wavelength λ.

4 Software

4.1 Programming Concepts

Part of the work towards this thesis has been development of software both for controlling all-sky cameras (Section 4.3) and for processing the images captured (Section 4.2). The software is written in a mixture of Python (cPython) and C. This section aims to give a brief introduction to some of the more abstract programming concepts and terminology used, which may otherwise be unfamiliar to the reader. It should be noted that some of the terminology used is specific to Python, however, the concepts are common to most object orientated languages.

4.1.1 Objects, Inheritance and Polymorphism

Object orientated programming is an attempt to better represent "real-world" entities within a program. Rather than forcing the programmer to use a limited number of data types such as integers and lists to model their problem, object orientated languages allow the creation of custom types, known as classes. A specific instance of a class is called an object, for example "2" is an instance of the integer class.

Objects are best thought of as independent "black-box" machines, essentially made up of two parts: attributes and methods. Attributes are data that belong to the object, and methods are functions that make the object do something. These are perhaps best demonstrated by example. Consider a class to represent an image, this might have an attribute to hold the pixel data and another attribute to hold the size of the image. Its methods might include a resize method and a rotate method.

Procedural programmers may argue that such a representation is possible without the need for objects. However, the real benefit of using objects comes with inheritance. Inheritance provides a mechanism for categorisation of objects, allowing a more natural approach to problem solving and a high degree of code re-use. Following on from the example above, consider that having written the image class we now wish to represent an all-sky image. Clearly an all-sky image is still just an image, but there are some operations specific to all-sky images that we might like to perform, for example aligning the top of the image with north. Rather than writing an all-sky image class from scratch, it can inherit from the image class, giving it all the associated attributes and methods, leaving us with just the align-north method to define. Not only does this mean that the code from the image class is reused, but also that we can use an all-sky image object at a more general level of classification i.e. as though it were an image object. Using objects effectively in this way requires polymorphism; allowing a single definition to be used with different types of data. For example, $1 + 2 = 3$, "aa" + "bb" = "aabb", in this case the addition operator is polymorphic, since it works for both integers and strings. As a dynamically typed language, Python is inherently polymorphic and therefore programs written to operate with image objects will also work with all-sky image objects.

The relationships between objects are often visualised using the Universal Modelling Language (UML). Fig. 7 shows the above example as a UML diagram.

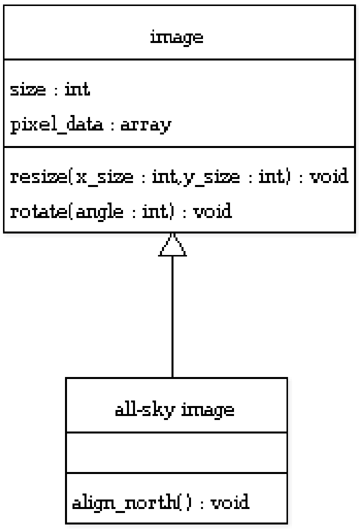

Figure 7: UML diagram showing the relationship between the image and all-sky image classes used as an example in the main text. The image class is a generalisation of the all-sky image class.

4.1.2 Parallel Processing

During the past few years, it has become increasingly common for computers to have either multiple processors, multi-core processors or both. Such systems are capable of truly parallel processing, executing many tasks (one per CPU core) at the same time. However, in order to achieve any performance gain, programs must be explicitly written to exploit the parallelism in the problems they are designed to solve. There are two commonly used approaches to achieving parallel processing in programs: multiple threads and multiple processes.

The definition of threads and processes is beyond the scope of this report. However, it is important to realise the differences in how they can be used in a program. Threads share their memory space, whereas processes do not. This means that changes made to a variable by one thread will be visible to another thread. Processes can be thought of more like separate programs, where one process knows little or nothing about what another process is doing. In general, this makes inter-thread communication easier to implement than inter-process communication. However, great care must be taken to synchronise threads properly, to prevent resource conflicts. For example, consider the process of incrementing a variable; it must be read from memory, incremented and then written back to memory. If multiple threads must increment the same variable, then it is possible that between one thread reading the old value from memory and writing the new value back, that another thread will have completed the entire process:

Thread 1 Reads value of variable: $i = 0$
Thread 1 Increments value: $i + 1 = 1$
Thread 2 Reads value of variable: $i = 0$
Thread 2 Increments value: $i + 1 = 1$

Thread 2 Writes value back to memory: $i = 1$
Thread 1 Writes value back to memory: $i = 1$

Despite having been incremented by two threads, it appears that the variable has only been incremented once. Such synchronisation errors can be avoided by using synchronisation primitives such as locks, which force threads to wait for each other. However, in Python, the recommended method of synchronisation is through the use of first-in-first-out (FIFO) queues. These can safely have multiple producer and/or consumer threads. Tasks can be parallelised (processed asynchronously) by placing them in a queue with multiple consumer threads. Alternatively, tasks from multiple producer threads can be processed synchronously by placing them into a queue with a single consumer thread.

Due to the internal workings of the cPython interpreter, true parallelism cannot be achieved using multiple threads. Whilst threads appear to execute concurrently, in fact only one thread executes at a time. Performance gains on multi-core systems can therefore only be achieved using multiple processes.

4.1.3 Shared Objects

Shared objects are one method of inter-process communication. A shared object can be thought of as occupying a space in memory shared between multiple processes. Method calls and attribute changes made by one process will be reflected in all processes. Of course the shared object is really an abstraction. In fact, each process is passed a proxy object, which has the same interface as the real object. Method calls and attribute changes to the proxies are communicated to the real object via a pipe, with changes being reflected in all the proxies.

4.2 The Python All-sky Image Library

All-sky images, particularly mono-chromatic ones, are difficult to interpret in their raw state. A significant amount of post-processing is typically required before they can be analysed effectively. Much software for working with all-sky images already exists. However, it largely consists of stand-alone scripts that process data from a specific camera in a certain way. The scripts allow little or no flexibility in processing options and are awkward to modify in order to work with different data. This makes it very difficult to compare data between different instruments. What is required is a more generalised piece of software, that can be easily extended to cope with images from any all-sky camera.

In an attempt to overcome the shortcomings of previous all-sky image processing code, we developed the Python All-sky Image Library (PASKIL). It provides a collection of functions and classes which can be used in users' own scripts to manipulate all-sky images. The processing details are left for the user to specify, allowing changes to be made without editing the source code. A plug-in architecture allows the library to be used with data from any all-sky imager. Scripts written using the library will therefore also work with any data set.

Full HTML documentation for PASKIL can be generated automatically from the source code[2] using the pydoc program. However, a brief overview of its key features is also given here.

---

[2] The PASKIL project is hosted on Google Code: `http://code.google.com/p/paskil/`

4.2.1 Loading Images

Broadly speaking, all-sky image data can be split into two parts: the image data itself, and the associated meta-data. In order to be able to cope with images and meta-data of all formats, PASKIL uses a plug-in architecture to convert the data into its own internal type, an allskyImage object. Support for images from a particular all-sky camera simply requires a plug-in to be written for that camera.

Each plug-in class has two methods: a test method, and an open method. The test method determines whether the plug-in can open a particular image and the open method returns an allskyImage object containing the image data and its associated meta-data. The image data is read using the Python Image Library (PIL), which itself uses a plug-in architecture to open images of different types. Common image formats are supported natively, and custom plugins can easily be written to provide support for more obscure formats. Support for proprietary raw image formats, such as those used by major camera manufacturers, is provided by PASKIL's cRaw module. This is capable of decoding the majority of raw image formats and loading them into PASKIL. Fig. 8 shows the structure of PASKIL's loading system.

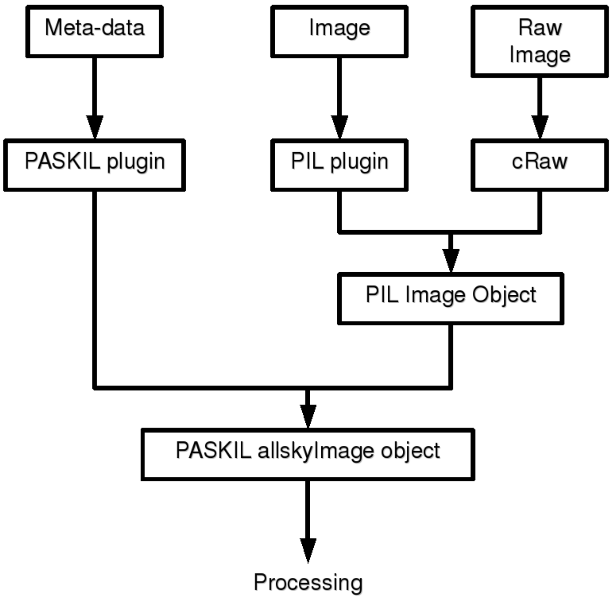

Figure 8: Flow chart showing the layer of abstraction provided by the plugin system between the core image processing code and the raw data.

4.2.2 Decoding NEF Files

The Nikon D80 camera is capable of producing images in both the Joint Photographic Experts Group (JPEG) format and Nikon Electronic Format (NEF).

The former is of limited use for scientific purposes since the compression techniques employed by the JPEG format are lossy. NEF is a lossless, TIFF (Tagged Image File Format) based file format which is used to store raw CCD data. The pixel data stored in NEF files is largely unprocessed, making it useful for scientific studies.

NEF is a proprietary format, with no publicly available documentation and as such is difficult to work with. However, open source projects such as dcraw [Coffin, 2007] and DeNEF [Stephens, 2007] have made decoding NEF files possible. The first step in decoding NEF files is decompression. NEF employs a compression technique very similar to the Huffman algorithm. Each pixel value is replaced with a unique encoding, whose length is based on the frequency of occurrence of that pixel value [MacKay, 2003]. In this way, the 16 bit pixel values[3] that occur most frequently in the image can be stored in a just a few bits. The disadvantage of storing some pixel values in less than 16 bits, is that other pixel values must be stored in more than 16 bits to ensure unique decodability. However, since longer encodings are assigned to less frequently occurring pixel values, the overall result is a reduction in file size. For a typical all-sky image, the compression achieves an 80% reduction in file size. Crucially for calibration, the Huffman algorithm is lossless, meaning that compression-decompression cycles leave the data unchanged. The header data in NEF files contains the probability tree used to map pixel values to their Huffman encodings. This information allows the reverse operation, decompression, to be performed.

The second step in decoding NEF files is interpolation. Each pixel of the CCD records the intensity of incoming light within a certain wavelength range. This is determined by a Colour Filter Mosaic (CFM) mounted in front of the CCD. The D80 camera uses a Bayer filter as its CFM (Fig. 9). This is made up of 2×2 sub-mosaics comprised of one red, one blue and two green filters in a G,B,R,G configuration. Each pixel records the intensity value of its specific colour as a 16 bit integer. The intensities of the other colours for a particular pixel are found by interpolating the values from neighboring pixels post-capture. The interpolation method used for this report is the Threshold-based variable number of gradients method [Chen, 2008]. This works by calculating the gradient in colour values in different directions in a 5×5 neighbourhood centred on the pixel under consideration. A threshold is then used to select a subset of directions that have a low gradient (and therefore a similar colour to the centre pixel). Weighted averages of colour values of the pixels in the subset are then used as the missing colour values for the centre pixel. The two green channels are interpolated separately.

All NEF file decoding done for this report was done using a modified version of the dcraw program. The decompression and interpolation routines have been left unchanged. However, the overall program structure has been changed to that of a shared library, and additional functions have been added to allow compilation as a Python extension module. This not only permits easy integration of dcraw's raw image support into PASKIL (Section 4.2) but also allows access to the raw CCD data from all four colour channels.

---

[3] The CCD is only capable of 12 bit intensity resolution, but the vaules are stored as 16 bit integers in the NEF files.

	0	1	2	3	4	5
0	G	B	G	B	G	B
1	R	G	R	G	R	G
2	G	B	G	B	G	B
3	R	G	R	G	R	G
4	G	B	G	B	G	B

Figure 9: Diagram of the Bayer filter used in the Nikon D80 showing the pixel colours at different coordinates on the CCD.

4.2.3 Colour Tables

Many all-sky cameras capture monochromatic images. In such images, it is often difficult to distinguish between regions of different intensity. Furthermore, most cameras store 12 bit intensity data in a 16 bit image, resulting in a completely black image with most viewing software.

Applying false colouring to the image, where each intensity value is represented by a different colour, solves both these issues. However, the colour table (the mappings between intensity and colour) must be chosen carefully. A linear colour table will hide much of the detail in the image. In order to show as much detail as possible, PASKIL creates colour tables based on the histogram of the image. Intensity ranges with a high pixel count are assigned larger colour ranges than intensity ranges with small numbers of pixels. Fig. 10 shows an image histogram and the corresponding non-linear colour table.

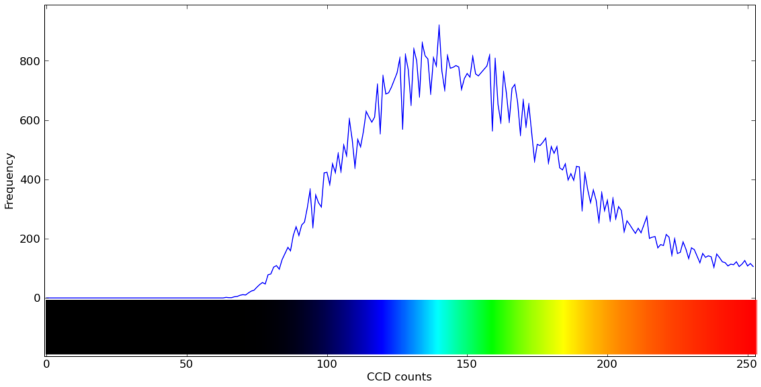

Figure 10: Histogram for an 8bit image showing the colour mappings for the different intensities as chosen by PASKIL. Note that the intensity ranges representing the highest numbers of pixels are given the largest range of colours.

4.2.4 Flat Field Calibration

The sensitivity of an all-sky camera has a dependency on the incident angle of the incoming light. This is largely due to the angular dependence of the transmission through the lens. The transmission is highest at zenith, falling away rapidly at high angles. However, the effect is partly offset by the difference in atmospheric volume being imaged. At higher angles from zenith, a greater volume of the atmosphere is being imaged, and therefore a greater intensity is expected.

One method of calibrating for the angular dependence of the camera system is suggested by Gulbrandsen [2006]. In this method, images taken during approximately uniform illumination of the sky (for example on cloudy days) are analysed. The intensities at different angles from zenith are recorded and averaged over several images. The resulting intensity/angle relationship is then used to calibrate for the angular dependence. Other methods of flat field calibration are discussed in Section 5.2.

PASKIL provides functionality for implementing the Gulbrandsen method of flat field calibration. Suitable images are found by comparing the variance in intensity. Periods of low variance indicate uniform illumination. For each selected image, slices through the centre of the image between 0-359 degrees from North at one degree resolution are taken. The intensities of pixels along the strip and their corresponding angles from zenith are recorded. The intensities are then binned by angle, with a resolution of one degree. The normalised median intensity for each bin is used as the calibration factor.

4.2.5 Keograms

One of the major challenges in interpreting all-sky images is dealing with the large volume of data. Typically, ASI systems capture images several times a minute, producing hundreds of gigabytes of data in a single field season. It is extremely time consuming to search through such data for events of interest. Furthermore, since each image is representative of conditions during a very short (a few seconds) time period, it is difficult to study events occurring over a larger temporal scale.

A common solution to this problem is to create keograms from the images [Eather et al., 1976]. This is done by taking a thin slice of pixels from the centre of each image, and stacking them together along a horizontal time axis as shown in Fig. 11. The slice is usually taken along the geomagnetic meridian.

PASKIL offers two methods of keogram creation: a cut and paste method, and an averaging method. The former method stacks the entire two dimensional slice from each image into the keogram. This is incorrect, since the width dimension of the slice is being plotted on a time axis, when in fact it represents angle from zenith. However, provided that the width of the slice is small compared to the width of the keogram, this error is negligible. The averaging method reduces the slice to one dimension by averaging across its width before it is added to the keogram. Larger slice widths can then be used, meaning that a greater proportion of the sky is summarised in the keogram. However, in practise there is little difference between the results produced by each method, as shown in Fig. 12.

4.3 Control Software

The task of controlling an ASI system can, broadly speaking, be subdivided into four key parts: user interface, camera interface, scheduling and post-capture processing. The software provided by Nikon for computer control of the D80

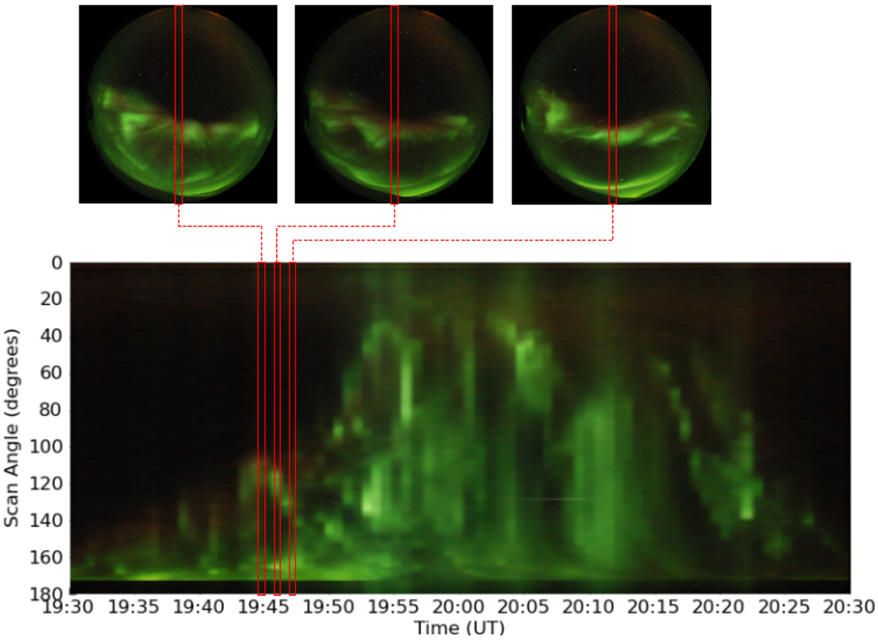

Figure 11: Keogram created from JPEG images from the Nikon D80 at KHO on December 23rd 2008, showing how the keogram is built up of slices five pixels wide, taken from the images along the geomagnetic meridian. 78 images were used to create the keogram.

can fulfil the first two of these parts. However, as a closed-source, graphical application it is extremely difficult to interface the Nikon software with other software to fulfil all parts. Instead, control software for the D80 at KHO was developed from scratch.

gPhoto2 is used as the interface to the camera. This is an open-source program which allows control of digital cameras via the Picture Transfer Protocol (PTP). As such it can be used for a wide variety of cameras and some effort was made in designing the control software to maintain this generality. In addition to enabling capture/download of images, gPhoto2 also allows camera settings such as exposure time to be set. The control software allows these settings to be tied to the scheduling, for example, allowing the exposure time to be adjusted dynamically with Sun elevation angle. The scheduling of the camera can be set based on date, time, Sun and Moon elevation angle and Moon phase. In addition to the camera settings, outputs can also be tied to the scheduling, allowing different post-capture processing options depending on the scheduling parameters.

An overview of the scheduling, capture and post-processing sections of the program is given in Fig. 13. The camera settings and output options are encapsulated by the CaptureMode class. A Scheduler object evaluates the scheduling parameters and passes the relevent CaptureMode object to the CaptureManager. This oversees the capture and downloading of images and constructs an OutputTask object for each image. The OutputTask contains all the informa-

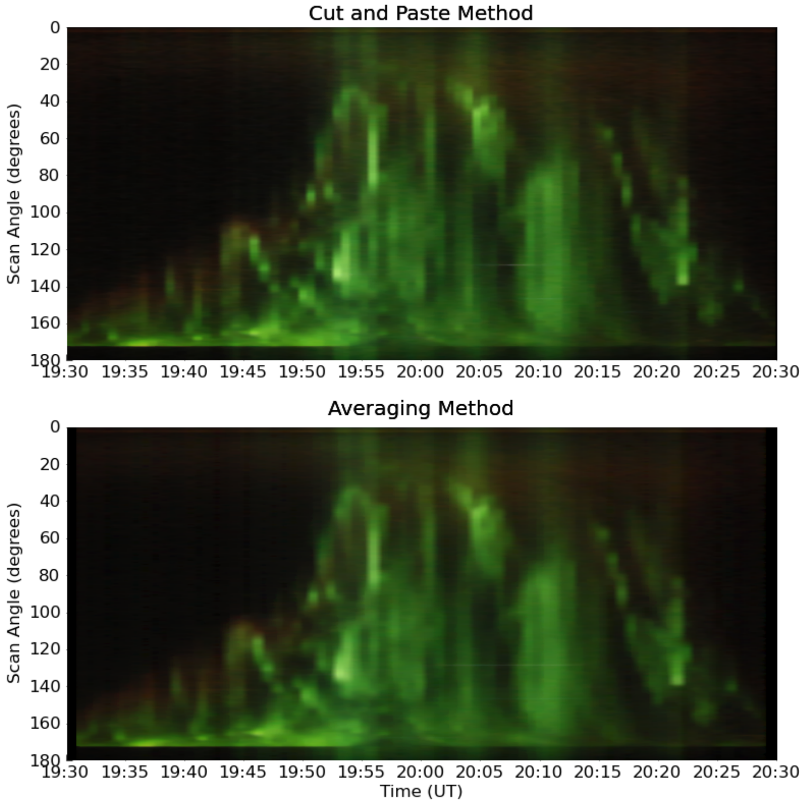

Figure 12: Keograms created from JPEG images from the Nikon D80 at KHO on December 23rd 2008, showing the difference between the cut and paste method (upper) and the averaging method (lower). Both methods produce almost identical results. Slice widths of 5 pixels and 25 pixels were used for the cut and paste and averaging methods respectively.

tion needed to create the outputs specified in the CaptureMode. Finally, the OutputTask object is passed to the OutputTaskHandler, which is responsible for creating the outputs in parallel via multiple processes. The post-capture processing operations themselves largely come from PASKIL.

The majority of the classes operate within their own thread. Method calls from external threads are queued and then executed by the class's own internal thread. This functionality is provided by inheritance from the ThreadQueueBase class and allows tasks to be easily serialised or parallelised. For example, the camera is a serial device and therefore method calls to the CameraManager class from multiple threads must be executed sequentially. On the other hand, production of multiple outputs can be performed asynchronously, and therefore method calls to the OutputTaskHandler class are executed in parallel across multiple processes.

The use of multiple processes for parallel output production necessitates a further layer of complexity. Classes which are used by the output production routines, must be both thread-safe and process-safe, meaning that they can be accessed by multiple threads and processes simultaneously without synchronisation problems. Inheritance from the ThreadQueueBase class deals with threading problems. Multi-process capabilities are realised using a combination of shared objects and proxies. Child processes are passed a proxy to the master object. Method calls to the proxy are passed to the master via a shared queue object, executed by the master's internal thread and the results passed back to the proxy via another shared queue. Proxy classes also inherit from ThreadQueueBase to make them thread-safe.

4.4 Summary of Capabilities

The previous few sections concentrated on the technical aspects of the software developed. This section provides a summary of the capabilities of the software, concentrating on the functionality rather the implementation.

4.4.1 PASKIL

PASKIL is organised into twelve different modules, each of which deals with a specific aspect of all-sky image processing. The key functionality of each module is summarised below.

allskyCalib Produces flat field calibration curves using the Gulbrandsen method.

allskyColour Creates colour tables for mapping grey-scale images to RGB images. The colour tables are intelligently stretched to pick out the most detail in the image.

allskyData This module is designed to ease the use of large data sets. It provides an abstraction layer between the user and the directory structure of the data set, allowing image access by capture time rather than file name.

allskyImage This is the main PASKIL module. It provides all the basic functionality for manipulating all-sky images: resizing, background subtraction, field of view cropping, alignment with north, basic filtering, adding a timestamp to the image and applying the flat field corrections and colour tables produced by the other modules. It also allows images to be saved (along with their corresponding meta-data) as either a Portable Network Graphics (PNG) file or a Flexible Image Transport System (FITS) file.

allskyImagePlugins Provides the plug-in architecture (see Section 4.2.1) that PASKIL requires to open different formats of all-sky image.

allskyKeo Deals with creation and manipulation of keograms. Intensity profiles can be generated at set angles or times. This module also provides specific functionality for producing keograms in real-time.

allskyPlot Plots keograms and images with colour bars.

allskyProj Produces map projections of all-sky images. Almost any projection is possible.

allskyRaw Provides functions for decoding raw image formats such as Nikon's NEF format. Most proprietary formats are supported.

misc and stats These provide a few miscellaneous functions that are used internally by the other modules.

4.4.2 Control Software

The key functionality of the control software may be summarised as follows:

- Complete control of all cameras supporting the PTP interface, including image capture/download and changing settings such as exposure time, ISO etc.
- Flexible capture scheduling based on Sun elevation, Moon elevation and phase, date and time. The schedule is tied to the camera settings and the output production allowing different settings to be applied and different outputs to be produced depending on the scheduling parameters. For example, the exposure time can be reduced during full moon periods.
- Realtime, parallel output production. Outputs are produced using PASKIL allowing a wide range of possibilities (see Section 4.4.1).
- All functionality can be accessed through a plain text settings file, without the need to edit the source code.
- Internally, all settings are managed by a single SettingsManager object. It is possible to register callback functions with the SettingsManager, which will be executed whenever a certain setting is modified. This allows the code to be easily extended, for example it makes adding a graphical user interface much simpler.

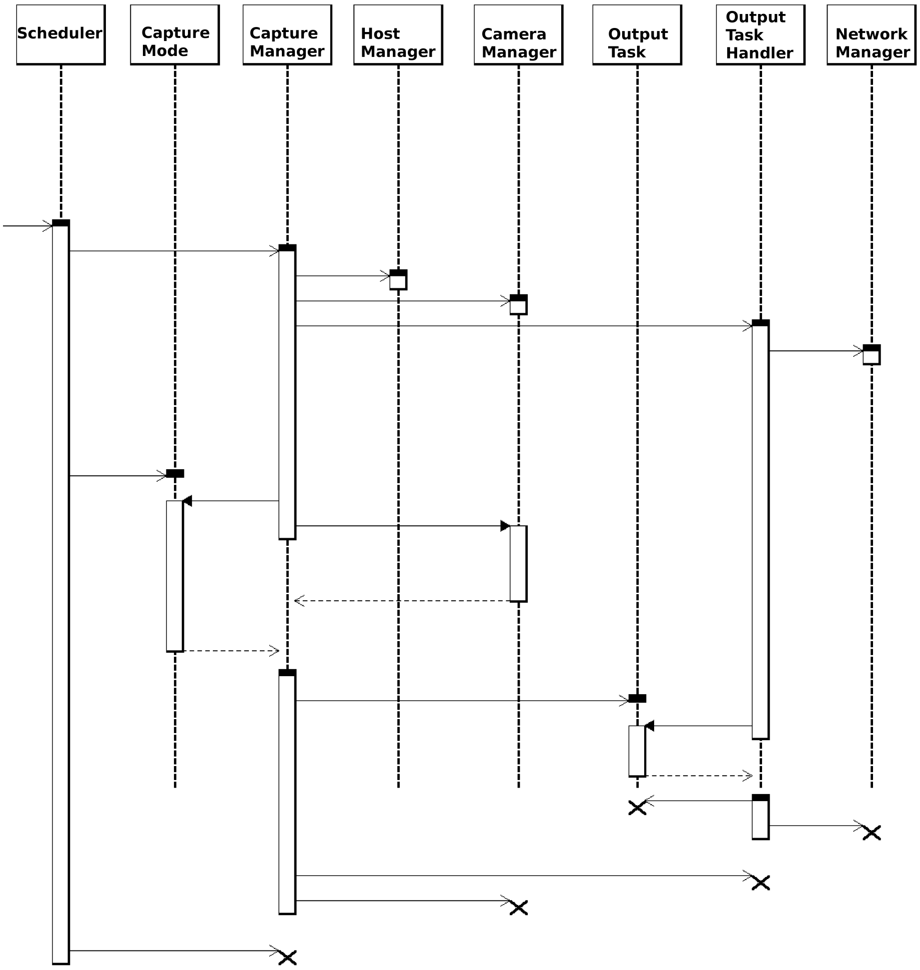

Figure 13: UML sequence diagram of the scheduling and output production parts of the DSLR control software. Open arrowheads indicate object instanciation, filled arrowheads indicate method calls and crosses indicate object destruction.

5 Calibration

Used as an RGB imager, the D80 can provide a useful overview of the sky. Cloud cover can be easily distinguished from aurora, as can snow and ice on the dome. However, to be used effectively as a scientific instrument, it must be possible to directly compare data from the D80 with other instruments. This can be achieved by calibrating the image data into absolute intensities. The standard intensity unit in auroral studies is the Rayleigh ($1R \equiv (1/4\pi) \times 10^6 photons\, cm^{-2} s^{-1} sr^{-1}$) [Baker, 1974]. Converting image data into Rayleighs is a multi-step process which requires many effects to be taken into account. A summary of the process is given below, and the steps are explained in more detail in the following sections.

1. All calibration is done using raw images (NEF files), since these contain unprocessed pixel data. The NEF files are decomposed into their separate colour channels using PASKIL (Section 4.2.2).
2. A background image is subtracted from each colour channel.
3. The pixel data is multiplied by a correction factor to account for absorption of light by the perspex dome that the camera is mounted inside (Section 5.1).
4. A flat field calibration is applied to account for the angular dependence of transmission through the lens (Section 5.2).
5. The spectral responsivity of the camera is calculated (Section 5.3).
6. Assuming a specific auroral emission dominates the image, the spectral responsivity is used to convert the pixel values to Rayleighs (Section 5.4).

5.1 Dome Transmission

When in operation, the DSLR is mounted inside a perspex instrument dome at KHO. During calibration, the camera was removed from inside the dome, and therefore the calibration measurements do not include absorption due to the dome. The transmission of different wavelengths through the dome was measured separately using the method outlined below.

Fig. 14 shows the experimental setup used. An Edmund Optics VIS-NIR Hyperspectral Spectrometer was mounted 7.5cm above a Lambertian diffuser. A flat section of perspex dome was mounted across the entrance slit of the spectrometer in such a way that light entering the instrument passed through the section at close to perpendicular incidence. The diffusing screen was illuminated using natural light. It was found that direct sunlight caused saturation of the spectrometer, even at its lowest integration interval. Instead, the measurements were carried out during a period of approximately even cloud cover. All measurements were made within a five minute period, during which the lighting conditions did not change significantly.

Three complete measurements of the transmission through the dome section between 400nm - 700nm (2.0nm bandwidth) were made. Each measurement consisted of a background scan with the spectrometer in a light proof bag, a

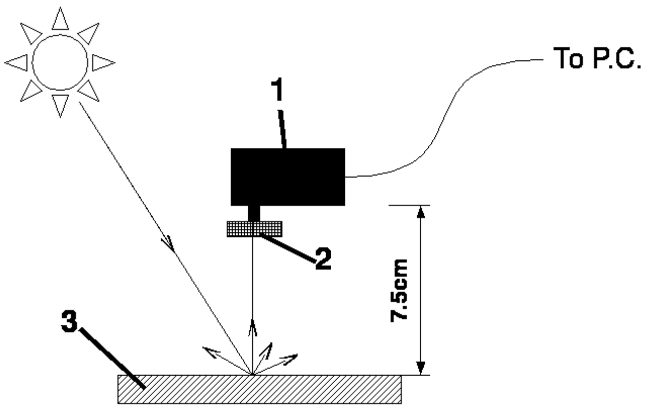

Figure 14: Experimental setup for measuring the dome transmission. (1) Edmund Optics VIS-NIR USB Hyperspectral Spectrometer, (2) Section of dome, (3) Lambertian screen.

scan without the dome section and a scan with the dome section in place. The mean transmission profile based on the three measurements is shown in Fig. 15.

As shown in Fig. 15, transmission through the dome is approximately independent of wavelength. It should be realised however, that this is a simplification of the effects of the dome. In practise, it is expected that the transmission properties of the dome will have some angular dependence and will also depend on the polarisation of the incident radiation. Accurate measurement of these properties is beyond the scope of this investigation, and we will assume a wavelength independent value of 96% for dome transmission.

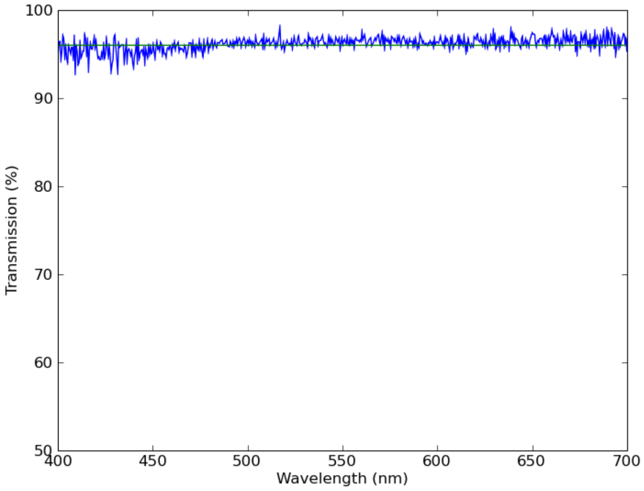

Figure 15: Percentage of incident light transmitted through a section of perspex instrument dome, as used at KHO. The 96% transmission line is also plotted, showing that it is a reasonable approximation over the full wavelength range.

5.2 Flat Field Calibration

As discussed in Section 4.2.4, it is possible to calculate a correction for the angular dependence of the sensitivity of the ASI system by analysing images taken under uniform illumination of the sky. However, the calibration curve found using this method includes the angular dependence of the atmospheric volume being imaged. Instruments such as the MSP (Section 3.1) do not include this effect in their calibration. A major objective of producing calibrated images from the DSLR system is to allow easy comparison with data from other instrumentation. Therefore it is important that the same factors are taken account of in the calibration. Whilst the flat field calibration method discussed in Section 4.2.4 is convenient, requiring only images recorded during cloudy periods, it is inappropriate in this case.

The standard method for flat field calibration is to find the angular dependence of pixel intensity in images recorded inside a large integrating sphere [Yamamoto et al., 2002, Shiokawa et al., 2000]. The sphere must be large enough to provide a uniform source across the entire field of view of the ASI under test. Variations in intensity must then be due to the ASI system itself. However, integrating spheres of this size are prohibitively expensive, and not widely available. The calibration for this report was conducted using a small integrating sphere as a uniform source, and rotating the camera system in order to image the source at different angles.

To avoid parallax shift when rotating the camera, it must be rotated about its centre of perspective. Whilst methods exist for accurately determining this point [Hamblenne, 2009], we have simply assumed that it lies at the front of the lens. Fig. 16 shows that this is a good approximation, with very little parallax shift occurring when the camera system is rotated about this point.

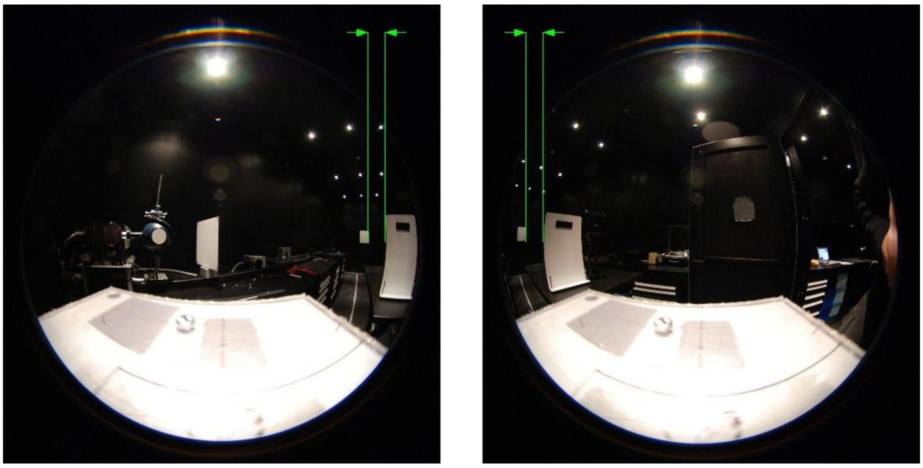

Figure 16: Images taken to validate the centre of perspective approximation of the camera system. The distance in the image between the near and far screens changes by 5 pixels when the camera is rotated by 150 degrees, less than a 0.2% parallax shift.

5.2.1 Experimental Setup

A Leica CLS 150 fibre optic illuminator is used as a light source for a HR320 CzerneyTurner spectrometer, providing a variable wavelength input into an integrating sphere. A second fibre bundle leads from the sphere to the FICS (Section 3.4). The D80 camera is mounted on a rotation stage, pivoting about the centre of perspective, at a distance of 59.5cm from the aperture of the sphere. The height of the rotation stage is adjusted such that the image of the integrating sphere's aperture appears approximately in the centre of the camera's field of view. Fig. 17 shows the experimental setup.

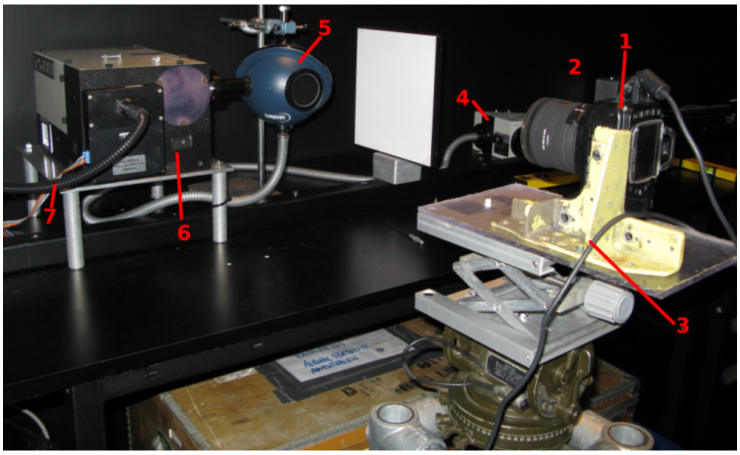

Figure 17: Experimental setup in the optical laboratory at UNIS for flat field calibration. In this picture the camera is set up for calibrating across the y-axis of the CCD. (1) Nikon D80 DSLR Camera, (2) Sigma EX circular fisheye lens, (3) Rotataion stage with centre of rotation at nodal point of camera, (4) FICS spectrograph, (5) Integrating sphere, (6) HR320 monochromator, (7) Fiber bundle from Leica 150W Tungsten Halogen lamp.

The flat field calibration was carried out for two source wavelengths: 537.47nm and 592.75nm (measured using the FICS). These correspond to the peak spectral responsivities for the green and red channels of the D80 respectively (Fig. 24). For each wavelength, two sets of images were taken, corresponding to rotation along the x- and y-axis of the CCD. Each set of images consisted of 34 images, taken at evenly spaced intervals across the entire 180 degree field of view of the camera. Fig. 18 shows a false colour, composite image of all 68 images for each wavelength.

All images were recorded at F2.8, four second exposure time and an ISO of 1600. The camera was set to record in NEF format and each image was decomposed into its four (RGBG) colour channels for analysis. The red channel was used for the calibration at 592.75nm and the first green channel for 537.47nm. All images had a background image subtracted from them before analysis.

5.2.2 Results

For each image, the relevent colour channel was extracted. The elliptical image of the integrating sphere's aperture was located in the image and cropped to

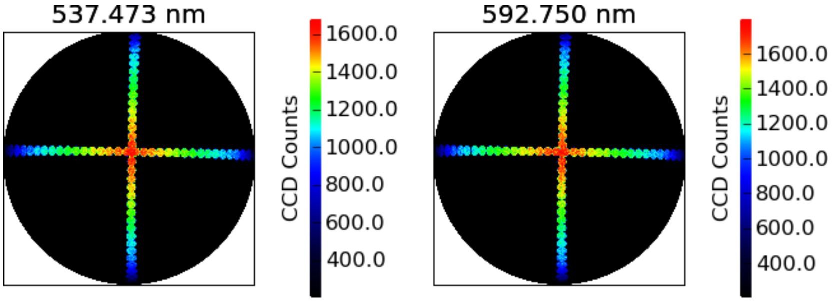

Figure 18: False colour plots of the images used for flat field calibration. Each ellipse in the plots represents a single image of the integrating sphere output at a different angle. The drop in recorded intensity towards high angles is clearly visible.

an ellipse 10 pixels smaller in all directions. This removes pixels from the non-uniform edge regions of the sphere's output. The intensities of the remaining pixels were then recorded and binned by angle from the centre with a one degree resolution. The mean intensity for each bin was calculated and normalised with respect to the mean intensity at zero degrees (Fig. 19).

The data show a linear decrease in transmission with angle out to 75 degrees from zenith. At higher angles, there is a much steeper fall off in intensity. There is no appreciable difference between the intensities recorded along the x and y axes of the CCD.

Also shown in Fig. 19 is the flat field calibration curves for the red and green channels calculated using the Gulbrandsen method (Section 4.2.4). The effect of the volume of atmosphere being imaged can clearly be seen, with the laboratory method predicting much lower intensities at high angles than the Gulbrandsen method. It can also be seen that while there is no discernible variation with wavelength of the data collected in the laboratory, there is a considerable difference when using the Gulbrandsen method. This is most likely due to light pollution from the mining installation close to KHO. This produces a high intensity red-biased (Sodium light) source towards the horizon. The errors due to light pollution further emphasise the shortcomings of this method for calibrations of this type.

For this report we assume a circularly-symmetric, wavelength independent, flat field calibration. This is formed by averaging over the x- and y-axis data measured in the laboratory from both wavelengths.

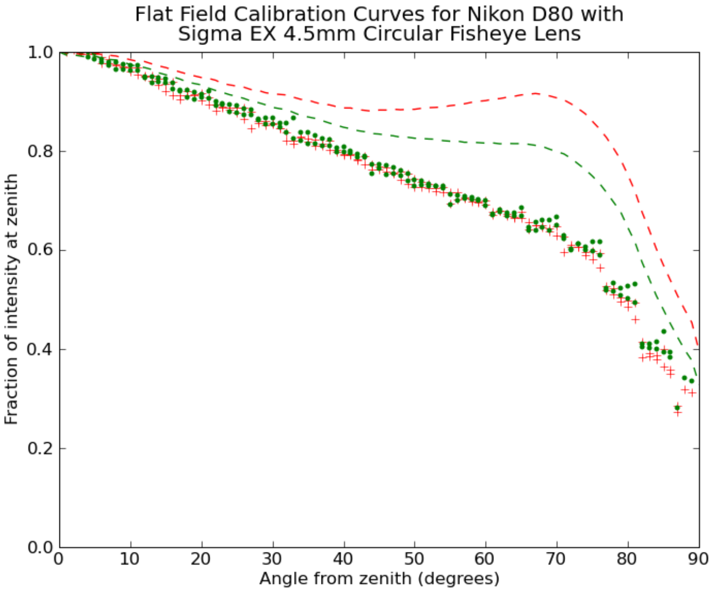

Figure 19: Flat field calibration curves for the D80 with a Sigma EX 4.5mm circular fisheye lens. Data are plotted for both the x and y direction calibrations. The crosses represent calibration using the red channel and a source wavelength of 592.75nm. The points represent calibration using the first green channel and a source wavelength of 537.47nm. The dashed lines show the curves calculated using the Gulbrandsen method on images captured between 05:00:26 - 05:59:32 UT on 29th January 2008 (63 images).

5.3 Spectral Responsivity

5.3.1 Method

The spectral responsivity of the D80 is found using a method based on the work of Sigernes et al. [2008]. In the calibrations carried out by Sigernes et al. [2008], a diffuse re-emitting screen illuminated by a monochromator was used. The non-uniformity of the illumination necessitated the assumption that the camera and the FICS observed the same area of the screen. This method has some severe limitations when applied to all-sky imagers. Firstly, the screen must fill the field of view of the camera, therefore it is not possible to use the same lens (fish-eye) for calibration as is used during operation. Differences in transmission profiles for each lens must then be taken into account, further complicating the calibration procedure. Secondly, the raw counts recorded by the camera must be summed over all pixels (to account for the non-uniform illumination), meaning that the calculated spectral responsivity applies to the CCD as a whole. Spatial distribution of intensity therefore, cannot be resolved. It is not possible to produce calibrated all-sky images using this method.

To overcome these limitations, we use an integrating sphere to provide a uniform illumination source. An integrating sphere is a hollow sphere with its internal surface coated with a diffusing, reflective material. The purpose of an integrating sphere is to spatially integrate radiant flux [Labsphere, 2009], providing a uniform source. To avoid having to recalibrate the FICS for use with the integrating sphere, a diffuser is mounted in the output port of the sphere. This provides a uniformly illuminated Lambertian surface, which can be imaged by both the camera and the FICS simultaneously.

Using the setup shown in Fig. 20, the height of the camera is once again adjusted to ensure that the aperture of the sphere appears in the centre of the field of view. The input fibre for the FICS is mounted 9.2cm from the sphere's aperture, ensuring that it fills the entire field of view. The wavelength of the sphere output is varied between 430nm-720nm with a total of 30 NEF images being recorded at approximately equal wavelength spacings. This wavelength range was chosen since below 430nm the signal to noise ratio of the FICS was too poor to resolve the source spectrum and the D80 is not sensitive to wavelengths above 720nm. An exposure time of four seconds, F2.8 and ISO 1600 was used. For each image, the spectrum of the source is recorded using the FICS spectrometer (Fig. 21). The FICS data is calibrated to R/Å as described in Section 3.4.

The image of the sphere's aperture was located in each image and the field of view cropped to exclude non-uniform edge pixels (as in Section 5.2.2). Each image was then decomposed into its four colour channels and the mean pixel value for each channel calculated. The mean was found by averaging over 6468 pixels. Fig. 22 shows the mean counts per pixel for each colour channel in all 30 images.

For a single colour channel, the raw counts recorded by a particular pixel can be expressed as:

$$I_R = \int F(\lambda) \cdot I_C(\lambda) \, d\lambda \tag{9}$$

Where I_R is the raw counts recorded by the pixel, $F(\lambda)$ is the spectral responsivity of the camera system and $I_C(\lambda)$ is the absolute intensity of the source.

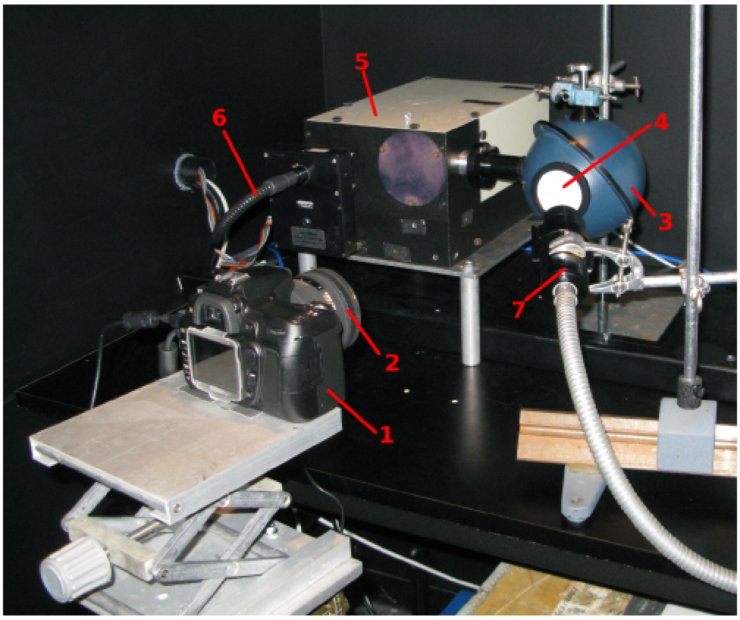

Figure 20: Experimental setup in the optical laboratory at UNIS for measuring spectral responsivity. (1) Nikon D80 DSLR Camera, (2) Sigma EX circular fisheye lens, (3) Integrating sphere , (4) Diffuser, (5) HR320 monochromator, (6) Fibre bundle from Leica 150W Tungsten Halogen lamp, (7) FICS spectrograph.

For a particular source spectrum, it can be assumed that the spectral responsivity is constant across the bandwidth of the source. Given the relatively narrow bandwidth of the source, this is a good assumption. The spectral responsivity can then be taken outside of the integral, leaving just the source intensity. For each image, this is evaluated by integrating the FICS spectrum across its full width. The spectral responsivity at each source wavelength can then be found using the matrix equation:

$$\mathbf{F}^T = \mathbf{C}^{-1} \cdot \mathbf{I_R}^T \tag{10}$$

Where $\mathbf{F}$ is a vector of the spectral responsivities at each source wavelength: $\mathbf{F} = (F_{\lambda 1}, F_{\lambda 2}, F_{\lambda 3}, \dots)$, $\mathbf{I_R}$ is a vector containing the counts per pixel at each wavelength: $\mathbf{I_R} = (I_{R\lambda 1}, I_{R\lambda 2}, I_{R\lambda 3}, \dots)$ and $\mathbf{C}$ is a diagonal matrix containing the absolute intensities of the source at each wavelength (I_A): $\mathbf{C} = diag(I_{A\lambda 1}, I_{A\lambda 2}, I_{A\lambda 3}, \dots)$

5.3.2 Results

This method of finding the spectral responsivity requires that the counts per pixel scale linearly with the intensity of the source and that this relationship is unaffected by exposure time.

A series of images were recorded with different exposure times. The mean counts per pixel per second were found (using the method outlined in Section 5.3.1) and it was found that the values were independent of exposure time provided that the CCD did not saturate.

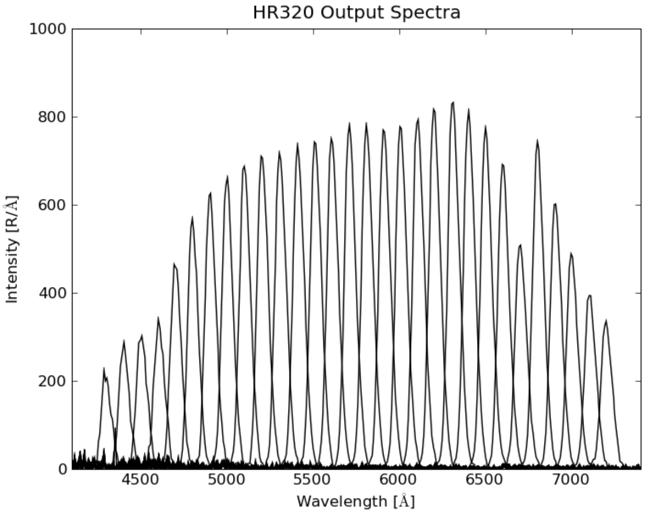

Figure 21: HR320 spectrometer output spectra. These correspond to the output spectra from the integrating sphere for the 32 images recorded.

The Leica 150W Tungsten Halogen lamp used as an illumination source has a variable size aperture. This allows the intensity of the output from the integrating sphere to be varied whilst keeping the wavelength constant. A series of images were recorded for different source intensities at 630.1 nm and 557.8 nm. For each image, the mean counts per pixel per second were found and plotted against the intensity of the source (Fig. 23). The data shows that the relationship between CCD counts and source intensity is, to a good approximation, linear.

Fig. 24 shows the calculated spectral responsivities of the D80's four colour channels at ISO 1600 and F2.8. Dayside and nightside auroral spectra recorded by the ASG at KHO are also plotted, these are discussed more in Section 5.4. The errors in wavelength correspond to the full-width at half-maximum of the source spectra. The errors in spectral responsivity are the standard errors in the mean counts per second per pixel.

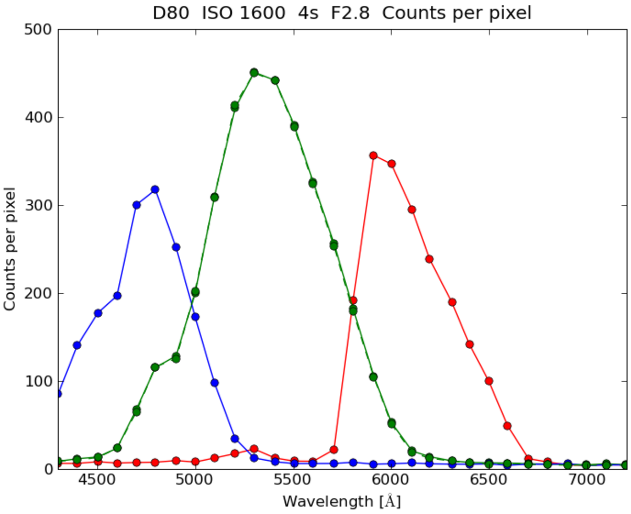

Figure 22: Mean raw counts per pixel for the four colour channels, averaged over 6468 pixels for a four second exposure at ISO 1600 and F2.8. Note that the raw counts for both green channels are almost identical.

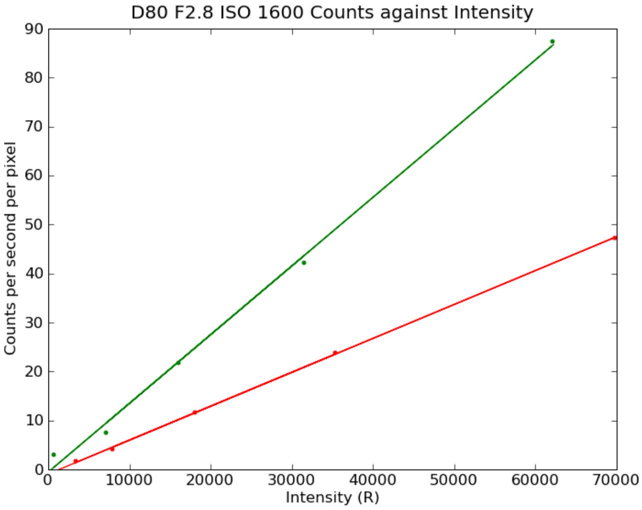

Figure 23: Counts per second per pixel against source intensity for a source of 630.1 nm and 557.8 nm for a four second exposure, F2.8 and ISO 1600.

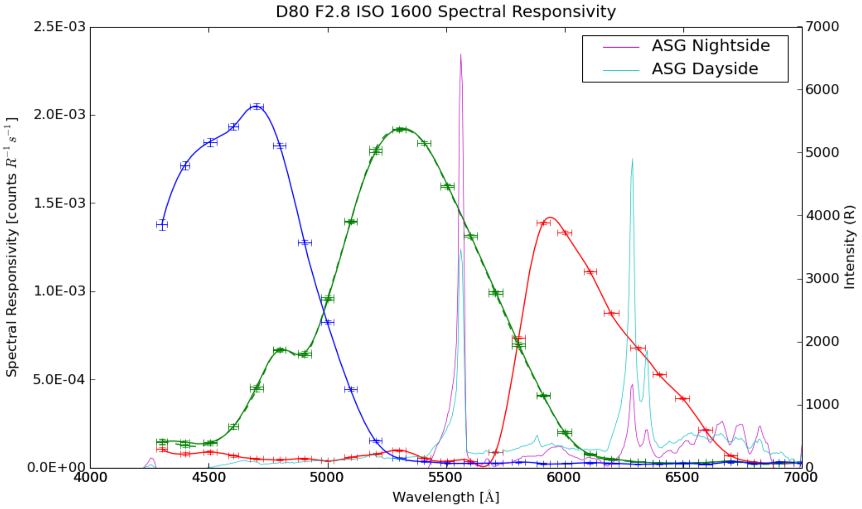

Figure 24: Spectral responsivities of the D80's four colour channels at ISO 1600 and F2.8. Also plotted are typical dayside and nightside auroral spectra recorded by the ASG (Section 3.3) at KHO.

5.4 Absolute Calibration

Typically, ASI systems use narrowband filters to allow them to image particular emissions within the auroral spectrum. However, as Fig. 24 shows, the separate colour channels of the D80 are sensitive to emissions across a wide range of wavelengths. According to Eq. 9, the CCD counts recorded by a single pixel will therefore be due to many different wavelength sources and the corresponding spectral responsivities of the camera. Such broadband intensity data is of little use in auroral studies. However, as mentioned in Section 2.3.2, the visible aurora is dominated by the atomic Oxygen emissions at 557.7 nm and 630.0 nm, and to a lesser extent the ionised Nitrogen emission at 427.78 nm. As the ASG data plotted in Fig. 24 shows, the D80 is sensitive to these wavelengths in different colour channels. By separating the pixel data into its separate colour channels, and assuming that the intensity recorded by each channel is only due to emissions at these particular wavelengths, it is possible to create calibrated images. We focus on the red and green channels (630.0 nm and 557.7nm emissions). The CCD counts of the red and green channels are converted to Rayleighs using the values of the spectral responsivities at 630.0 nm and 557.7 nm respectively.

In order to more accurately determine the spectral responsivities at these wavelengths, we use the CCD counts per second against intensity data presented in Fig. 23. The spectral responsivity is given by the gradient of the counts against intensity line. This gives a spectral responsivity of $(1.4 \pm 0.04) \times 10^{-3} counts\ s^{-1}\ R^{-1}$ for 557.7 nm and $(6.9 \pm 0.05) \times 10^{-4} counts\ s^{-1}\ R^{-1}$ for 630.0 nm. The error corresponds to the standard error in the linear regression performed to ascertain the gradient.

5.5 CCD Comparison

During the 2008-2009 field season the shutter mechanism on the D80 malfunctioned. Whilst it was being repaired, a new D80 was purchased and installed at KHO. The spectral responsivity of the new D80 was calculated using an identical experimental setup and method as for the first. The calculated spectral responsivities for the two D80s agreed within experimental error across the full wavelength range.

Whilst this is too small a sample to draw any firm conclusions from, the results do indicate a high level of consistency in the CCDs used in D80 cameras. It is therefore possible that for a large deployment of D80s, a single calibration could be performed and applied to data from all the cameras.

6 Example Data

At the time of writing, the D80 has been operating at KHO for two field seasons. Due to the ongoing development and testing work carried out during its operation, the data series recorded is somewhat incomplete. Furthermore, much of the data remains unprocessed for the same reasons. Despite this, the D80 has proved to be a useful instrument. It has been used during two rocket campaigns (SCIFER2 and ICI-2) where realtime data was used in conjunction with other instruments to assess the launch conditions. Data has also been used in a range of public presentations and outreach events.

This section presents a selection of data from the D80 recorded during the 07/08 and 08/09 field seasons. Focus is given to data that emphasises both the capabilities and shortcomings of the D80 system.

6.1 Substorm Evolution

Used as an RGB colour-composite imager, the D80 is capable of producing attractive, true-colour images of auroral events. These images are particularly easy to interpret, making them useful for public presentation and science outreach purposes. True colour images give an impression of what one would actually see during an auroral event. As an example, Fig. 25 shows the progression of a substorm. The images have been projected onto a map using PASKIL, making the poleward expansion of the auroral oval clear.

This particular event follows the typical progression of auroral substorms [Kivelson and Russel, 1995]. It begins as a quiet arc far to the South of Longyearbyen, Fig. 25(a). The intensification of a section of the arc shown in Fig. 25(b) marks the onset of the substorm, and this is followed by a rapid poleward expansion of the auroral oval, the expansion phase, Fig. 25(c) and Fig. 25(d). During the expansion phase, the oval also expands equatorward, although to a lesser extent than the poleward expansion. However, this is outside the field of view of the camera. Fig. 25(e) shows the subsequent breakup of the poleward region of the auroral oval, known as the recovery phase. This is shortly followed by a return to a quiet arc Fig. 25(f). The expansion, and subsequent retreat of the auroral oval can be seen clearly in Fig. 25(g) which shows a keogram of the entire substorm event.

6.2 Polar Cap Patches

As discussed in Section 2.4, polar cap patches are regions of enhanced electron density occurring at an altitude of approximately 300km. The polar convection cycle (Section 2.2.2) pulls patches from the dayside, across the polar cap and into the nightside auroral oval. Patches can be observed optically as weak airglow at 6300Å due to recombination of atomic Oxygen. However, their signature is typically very weak compared to the background, making them difficult to observe in all-sky images. Keograms provide a much clearer visualisation, with patches producing a distinctive reversed "S" signature in the nightside region. Fig. 26 shows data from the MSP's 6300Å channel on the 1st February 2008. Two patches are visible, entering the auroral oval at 22:00 and 22:20 respectively.

Fig. 27 shows all-sky data for the same time period as Fig. 26. The upper keogram shows data from the 6300Å channel of the UiO ASI, the lower keogram

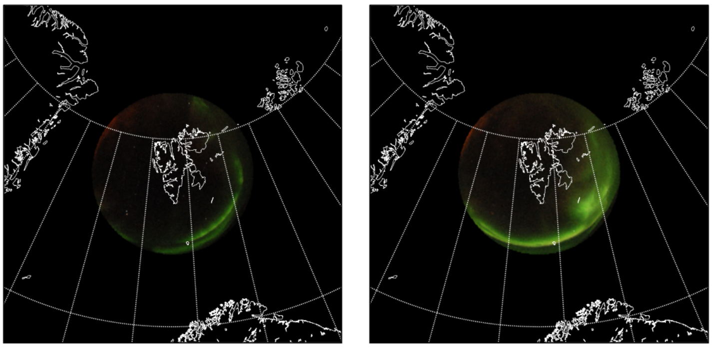

(a) 22:30:50 UT

(b) 22:35:38 UT

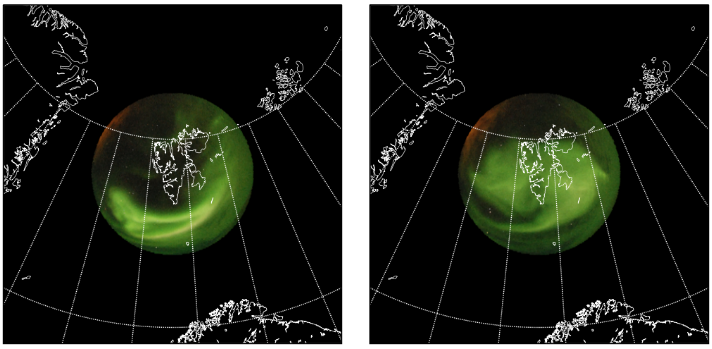

(c) 22:40:26 UT

(d) 22:45:15 UT

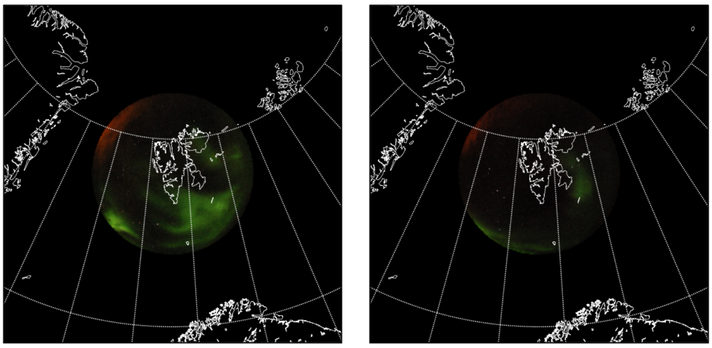

(e) 22:50:02 UT

(f) 22:55:50 UT

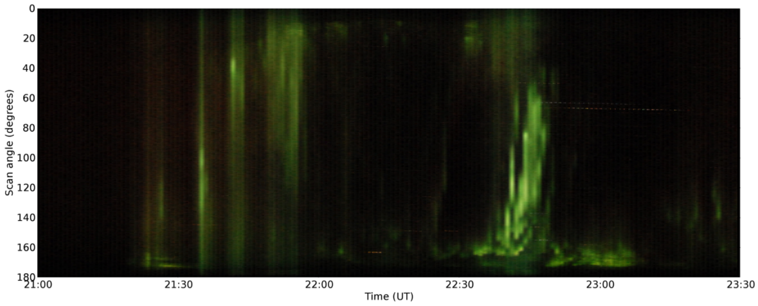

(g)

Figure 25: Evolution of a substorm as viewed by the D80, showing the initial quiet arc 25(a), the expansion phase 25(b)-25(d), the recovery phase 25(e) and return to a quiet arc 25(f). 25(g) shows a keogram made along the geomagnetic meridian of the entire event.

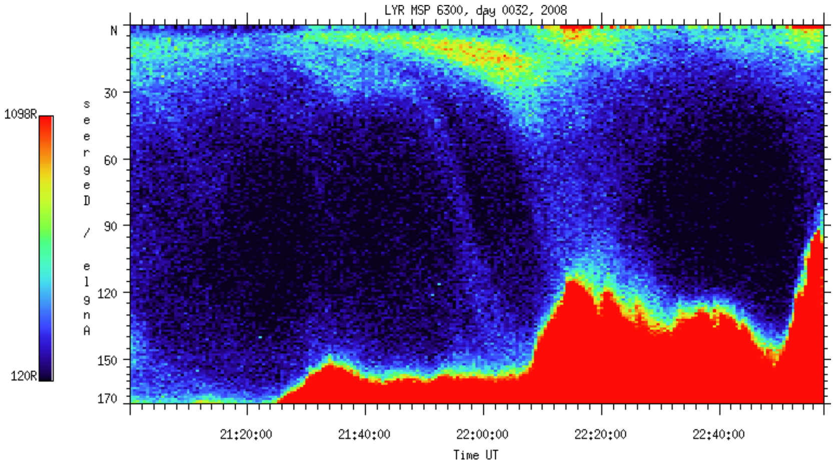

Figure 26: 6300Å MSP data from 1st February 2008 showing two polar cap patches.

shows data from the red channel of the D80. Whilst the polar cap patches are not as clearly visible as they are in the MSP data, they are still apparent in the UiO ASI data. However, they are not visible above the background noise in the D80 data.

Another interesting feature of the D80 data, is the relatively high intensity along the northern horizon compared to the UiO ASI data. This is due to light pollution from the nearby mining installation. The narrow bandwidth of the interference filters used in the UiO ASI remove the majority of this light. However, the D80 is in fact particularly sensitive to light at this wavelength. As is the case with most outdoor lighting, the majority of the lights at the mine are sodium vapour lights. These produce light at around 589 nm. Unfortunately, this is remarkably close to the peak in spectral responsivity for the D80's red channel (Fig. 24). This makes the red channel particularly susceptible to light contamination, and therefore of limited use in auroral studies at KHO, where light pollution is a problem when there is cloud cover.

6.3 Dayside/Nightside Comparison

As discussed in Section 2.3.3, the different mechanisms for ionospheric particle injection on the dayside and nightside result in contrasting emission profiles. In particular, dayside emissions are dominated by the 630.0 nm atomic Oxygen emission, whereas nightside emissions are dominated by the 557.7 nm atomic Oxygen emission. Fig. 28 shows intensity against time profiles for the 557.7 nm and 630.0 nm channels of the MSP at KHO for the morning of 10th January 2008, during a period of dayside auroral activity. As a comparison, Fig. 29 shows similar data for a period of nightside auroral activity recorded on the 1st February 2008. The data shows a clear dominance of 557.7 nm emissions on the nightside. Although the dayside data does not show so clearly the higher intensities of 630.0 nm emissions, it is still evident (with the exception of the high peaks in 557.7nm emission around 07:40 UT). The overall higher intensities in both channels on the nightside is also to be expected, due to the more diffuse

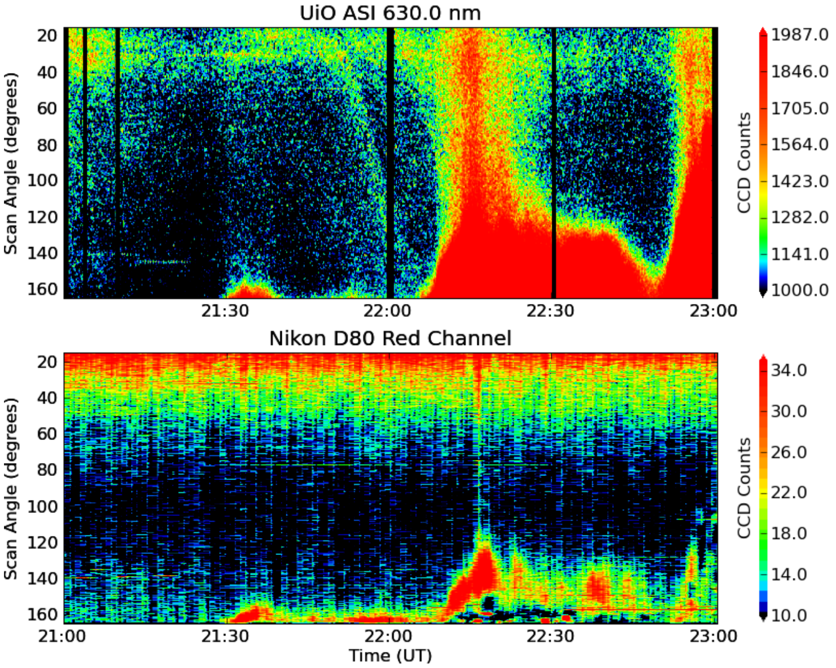

Figure 27: Keograms showing data from the UiO ASI's 6300Å channel and the red channel of the D80 for the same time range as Fig. 26. Although faint, the polar cap patches are visible in the UiO ASI data, but not in the D80 data.

nature of dayside aurora.

Calibrated intensity data from the D80 for the same time periods as the MSP data is shown in Fig. 30. To allow direct comparison with the MSP data, the intensity profiles were produced from keograms with a strip width corresponding to the field of view of the MSP perpendicular to the geomagnetic meridian (2° = 9 pixels). The keograms were produced using the averaging method (Section 4.2.5), and corrections for flat-field and dome transmission effects were applied.

Although the D80 data is in reasonable agreement with the MSP data, there are some discrepancies. Most notably, the peaks in 557.7 nm emission between 22:10-22:20 UT have a considerably higher intensity in the MSP data. Furthermore, the difference in intensity between the two higher peaks in the D80 data is not apparent in the MSP data. One possible explanation for these variations is the difference in time resolution between the MSP and the D80. While the MSP has a time resolution of 16 seconds, for the presented data the D80 was capturing one image a minute. For highly dynamic aurora therefore, we might expect that the D80 would not record much of the detail shown by the MSP.

The dayside data from the D80 is consistently 1-2kR higher than the corresponding MSP data. This is likely caused by the high background light levels. During this time period, the Sun was approximately 10 degrees below the horizon and was therefore providing at least some ambient light. Such broadband illumination is largely negated by the narrowband filters of the MSP, however not so for the D80 where it causes an almost constant offset. The slight increase in offset at later times corresponds to the increase in Sun elevation.

A further source of discrepancy between the two data sets may be the calibration of the MSP itself. The MSP at KHO is calibrated in-place by mounting a diffusing screen on the roof of the observatory above the entrance slit. A calibration lamp is then mounted at the far end of the roof, and the intensity recorded by the MSP. The fact that this calibration is largely performed outside, makes it more error prone than calibration in a laboratory. Accurate alignment of the screen and the lamp are more difficult and weather conditions, such as flurries of snow, can skew the measurements. A new calibration method for the MSP is currently under development, and will be used during the next (2009-2010) field season.

The major advantage of the D80 over the MSP is its ability to record the two-dimensional intensity distribution. Fig. 31 shows RGB and calibrated red and green channel images of both dayside and nightside auroral activity. The high background levels in the dayside images are clear, and the higher intensities to the south favour the argument that high Sun elevation is the cause of the overestimation of the intensities. In the nightside images, light pollution from the nearby mine is once again prevalent to the north, particularly in the 630.0 nm image.

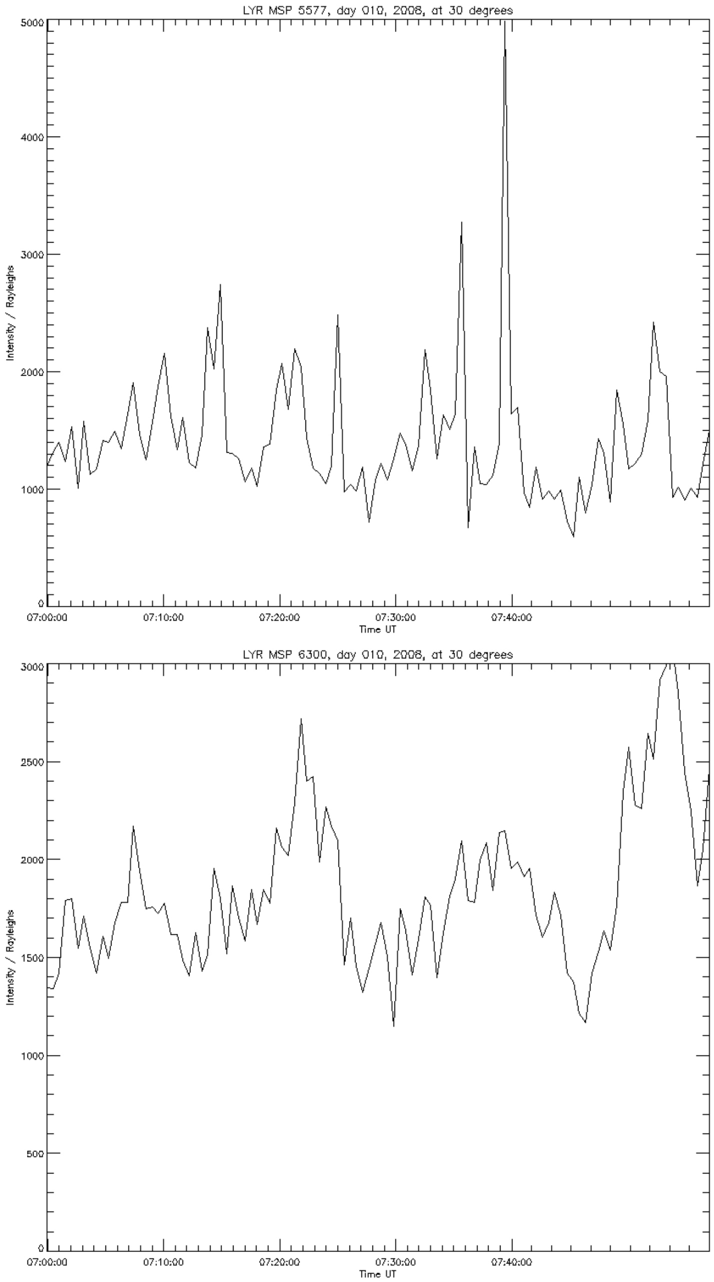

Figure 28: Intensity against time profiles for the 557.7 nm (upper) and 630.0 nm (lower) channels of the MSP at KHO, recorded on the 10th January 2008. The profiles are taken at 30 degrees from geomagnetic north (along the geomagnetic meridian).

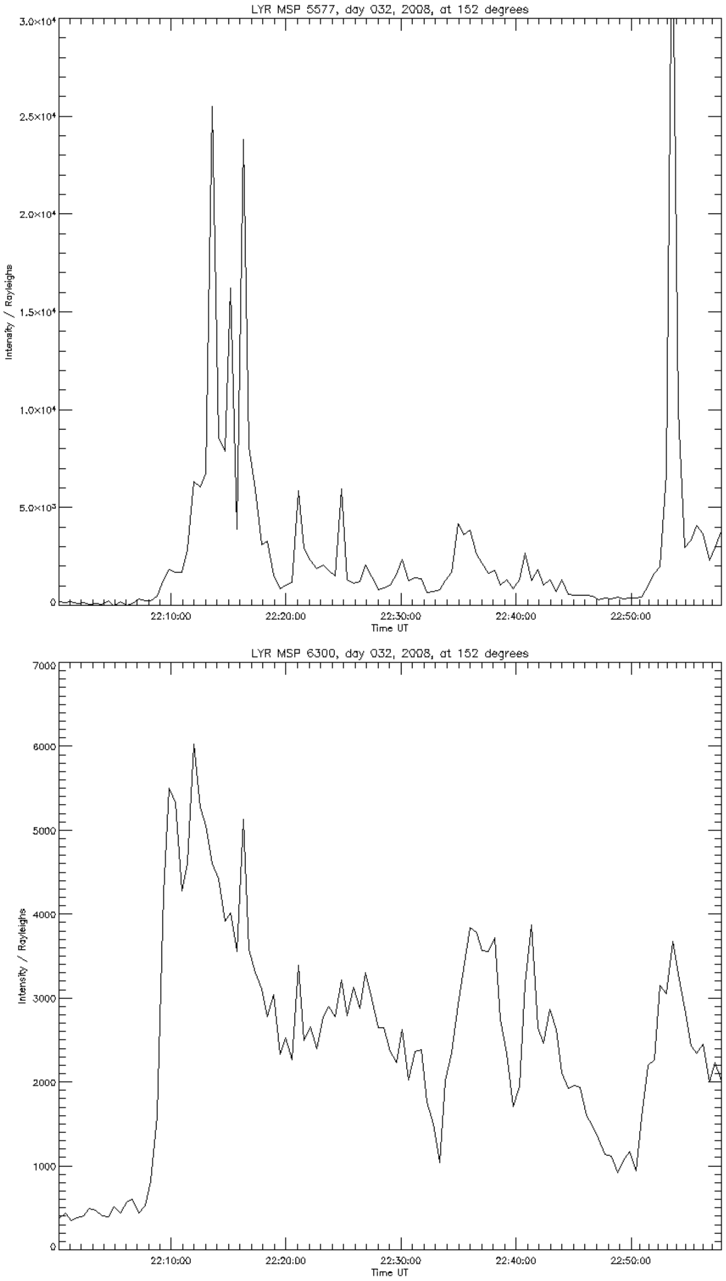

Figure 29: Intensity against time profiles for the 557.7 nm (upper) and 630.0 nm (lower) channels of the MSP at KHO, recorded on the 1st February 2008. The profiles are taken at 152 degrees from geomagnetic north (along the geomagnetic meridian).

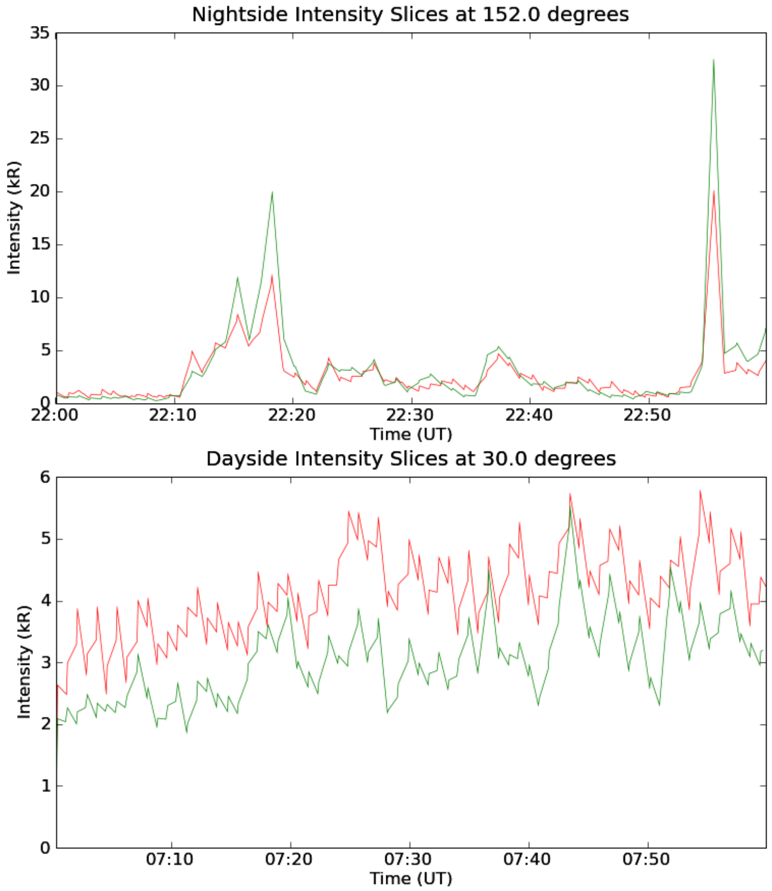

Figure 30: Intensity against time profiles for 557.7 nm and 630.0 nm emissions from nightside (upper) and dayside (lower) aurora. The nightside profile is taken at 152 degrees from geomagnetic north (along the meridian) and the dayside profile is taken at 30 degrees. Nightside data is from 1st February 2008 and dayside is from 10th January 2008.

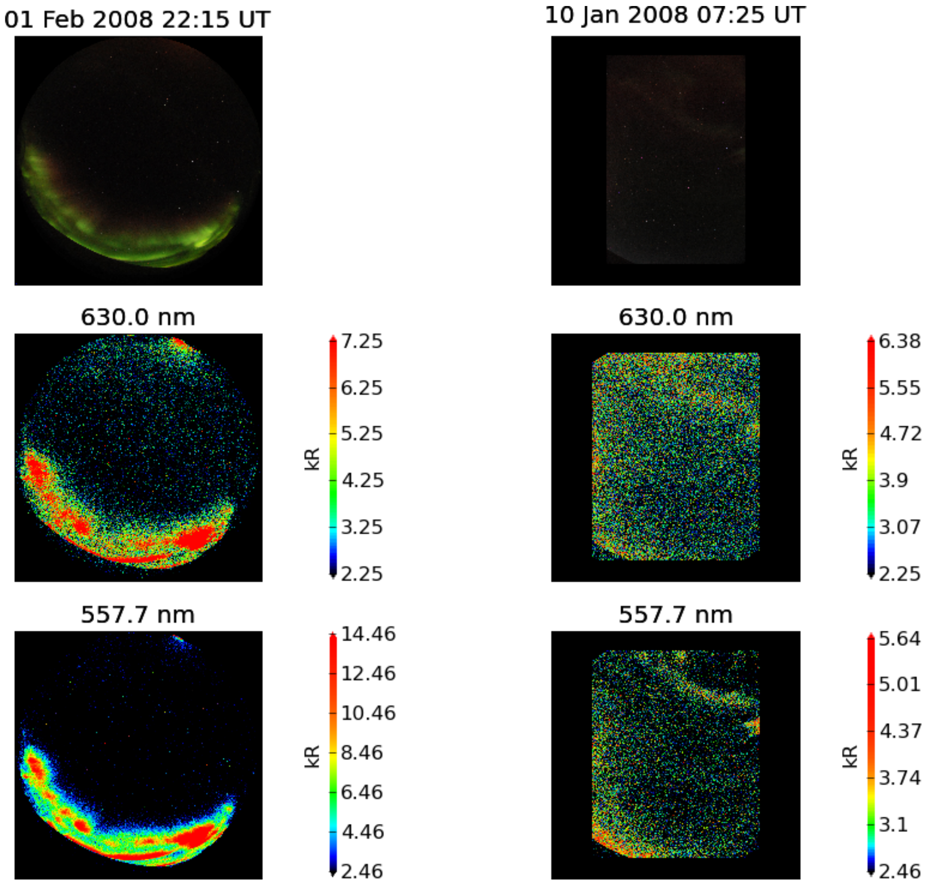

01 Feb 2008 22:15 UT

10 Jan 2008 07:25 UT

630.0 nm

557.7 nm

Figure 31: RGB and calibrated images showing nightside (left) and dayside (right) aurora. The dayside images were taken with a diagonal fisheye lens, hence the cropped field of view.

7 Concluding Remarks

This report has been an investigation into the use of commercially available DSLR cameras, specifically the Nikon D80, as cost-effective all-sky imaging systems. A general purpose software library for processing all-sky images was developed, allowing images from different cameras to be easily compared. Control software for scheduled time-lapse image capture was also created and has been used in the deployment of a Nikon D80 camera at KHO. The spectral responsivity of the D80 was found allowing images to be calibrated to absolute intensity units.

The principle findings of this investigation may be summarised as follows:

- True colour images produced by the D80 provide a clear overview of optical conditions. Cloud cover and snow/ice on the dome are more easily distinguished from aurora than in images from monochromatic ASIs. The ease of interpretation of such images makes them particularly useful for public presentation.
- The lack of intensification in the D80 allows it to be run safely in all lighting conditions, including periods of full moon. However, its ability to resolve low intensity features in the aurora is poor compared to intensified systems such as the UiO ASI. Polar cap patches, for example, are not visible above the background noise in data from the D80.
- The spectral responsivity of the D80 is such that the dominant auroral emissions (4278Å, 5577Å, 6300Å) are separated across the blue, green and red colour channels. This allows each colour channel to be calibrated to absolute intensity units.
- Calibrated intensities from the D80 show good agreement with MSP data. However, the difference in time resolution between the instruments cause discrepancies when imaging highly dynamic aurora. The broadband sensitivity of the D80 causes an overestimation of intensities when there is any ambient lighting, for example light pollution or high Sun elevation.
- D80 cameras are not designed for the type of continuous use that ASIs undergo. The shutter mechanism on the D80 malfunctioned after 304972 images. This is the equivalent of 106 days of continuous operation (one image every 30 seconds). Regular repair or replacement therefore seems inevitable when using DSLRs as ASIs.
- Despite their limitations, the low price of D80 cameras makes them an extremely cost effective solution for all-sky imaging. The apparent similarity in spectral responsivity between the CCDs in different cameras provides the opportunity to implement multiple systems with relative ease and low cost.

References

D. J. Baker. Rayleigh, the unit for light radiance. *Applied Optics*, 13(9):2160–2163, 1974.

A. Brekke. *Physics of the Upper Polar Atmosphere.* Wiley-Praxis, 1997.

T. Chen. Interpolation using a threshold-based variable number of gradients. `http://scien.stanford.edu/class/psych221/projects/99/tingchen/algodep/vargra.html`, feb 2008.

D. Coffin. dcraw. `http://www.cybercom.net/$\sim$dcoffin/dcraw/`, nov 2007.

G. Crowley. Critical review of ionspheric patches and blobs. *URSI Review of Radio Sci.*, 1996.

C. S. Deehr, G. G. Sivjee, A. Egeland, K. Henriksen, P. E. Sandholt, R. Smith, P. Sweeney, C. Duncan, and J. Gilmer. Ground-based observations of F region aurora associated with the magnetospheric cusp. *J. Geophys. Res.*, 85: 2185–2192, May 1980. doi: 10.1029/JA085iA05p02185.

J. Dungey. Interplanetary magnetic field and the auroral zones. *Physical Review Letters*, 6:4748, 1961.

R. H. Eather, S. B. Mende, and R. J. . R. Judge. Plasma injection at synchronous orbit and spatial and temporal auroral morphology. *J. Geophys. Res.*, 81(16): 2805–2824, 1976.

N. Gulbrandsen. Polar cap patch occurrence rate over svalbard and its dependence on IMF By. Master's thesis, UiO/UNIS, 2006.

A. Hamblenne. Method for a precise location of the entrance pupil on a dslr camera. `http://www.outline.be/quicktime/tuto/TheGrid.pdf`, jan 2009.

M. Kivelson and C. Russel. *Introduction to Space Physics.* Cambridge University Press, 1995.

W. C. Knudsen. Magnetospheric convection and the high-latitude f 2 ionosphere. *J. Geophys. Res.*, 79(7):10461055, 1974.

Labsphere, 2009. A guide to integrating sphere radiometry and photometry. Technical report, Labsphere Inc., 2009.

D. A. Lorentzen, N. Shumilov, and J. Moen. Drifting airglow patches in relation to tail reconnection. *Geophysical Research Letters*, 31:2806–+, Jan. 2004. doi: 10.1029/2003GL017785.

D. MacKay. *Information Theory, Inference, and Learning Algorithms.* Cambridge University Press, 2003.

P. T. Newell, J. M. Ruohoniemi, and C.-I. Meng. Maps of precipitation by source region, binned by imf, with inertial convection streamlines. *J. Geophys. Res.*, 109, 2004. doi: 10.1029/2004JA010499.

K. Oksavik, J. M. Ruohoniemi, R. A. Greenwald, J. B. H. Baker, J. Moen, H. C. Carlson, T. K. Yeoman, and M. Lester. Observations of isolated polar cap patches by the european incoherent scatter (eiscat) svalbard and super dual auroral radar network (superdarn) finland radars. *J. Geophys. Res.*, 111, 2006. doi: 10.1029/2005JA011400.

N. Partamies, M. Syrjaesuo, and E. Donovan. Using colour in auroral imaging. *Canadian Journal of Physics*, 85:101–109, Feb. 2007. doi: 10.1139/P06-090.

A. Rae. *Quantum Mechanics.* Institute of Physics Publishing, 4th edition, 2002.

P. E. Sandholt, C. J. Farrugia, J. Moen, Ø. Noraberg, B. Lybekk, T. Sten, and T. Hansen. A classification of dayside auroral forms and activities as a function of interplanetary magnetic field orientation. *J. Geophys. Res.*, 103: 23325–23346, Oct. 1998. doi: 10.1029/98JA02156.

K. Shiokawa, Y. Katoh, M. Satoh, M. K. Ejiri, and T. Ogawa. Integrating-sphere calibration of all-sky cameras for nightglow measurements. *Adv. Space Res.*, 26(6):1025–1028, 2000.

F. Sigernes, J. M. Holmes, M. Dyrland, D. A. Lorentzen, S. A. Chernous, T. Svinyu, J. Moen, and C. S. Deehr. Absolute calibration of optical devices with a small field of view. *J. Opt. Technol.*, 74:669–674, 2007.

F. Sigernes, J. M. Holmes, M. Dyrland, D. Lorentzen, T. Svene, K. Heia, T. Aso, S. Chernouss, and C. Deehr. Sensitivity calibration of digital colour cameras for auroral imaging. *OPTICS EXPRESS*, 16:15623–15632, 2008.

D. Stephens. DeNEF. `http://www.cheeseplant.org/$\sim$daniel/pages/denef.html`, nov 2007.

M. Yamamoto, M. Kubota, S. Takeshita, M. Ishii, Y. Murayama, and M. Ejiri. Calibration of CRL all-sky imagers using an integrating sphere. *Adv. Polar Upper Atmos. Res.*, 16:173–180, 2002.